A Chip for Hydrodynamic Microvortical Rotation of Live Single Cells

by

Jakrey R. Myers

A Thesis Presented in Partial Fulfillment
of the Requirements for the Degree
Master of Science

Approved June 2012 by the
Graduate Supervisory Committee:

Deirdre Meldrum, Chair
Roger Johnson
David Frakes

ARIZONA STATE UNIVERSITY

August 2012

ABSTRACT

Single cell analysis has become increasingly important in understanding disease onset, progression, treatment and prognosis, especially when applied to cancer where cellular responses are highly heterogeneous. Through the advent of single cell computerized tomography (Cell-CT), researchers and clinicians now have the ability to obtain high resolution three-dimensional (3D) reconstructions of single cells. Yet to date, no live-cell compatible version of the technology exists. In this thesis, a microfluidic chip with the ability to rotate live single cells in hydrodynamic microvortices about an axis parallel to the optical focal plane has been demonstrated. The chip utilizes a novel 3D microchamber design arranged beneath a main channel creating flow detachment into the chamber, producing recirculating flow conditions. Single cells are flowed through the main channel, held in the center of the microvortex by an optical trap, and rotated by the forces induced by the recirculating fluid flow. Computational fluid dynamics (CFD) was employed to optimize the geometry of the microchamber. Two methods for the fabrication of the 3D microchamber were devised: anisotropic etching of silicon and backside diffuser photolithography (BDPL). First, the optimization of the silicon etching conditions was demonstrated through design of experiment (DOE). In addition, a non-conventional method of soft-lithography was demonstrated which incorporates the use of two positive molds, one of the main channel and the other of the microchambers, compressed together during replication to produce a single ultra-thin (<200 μm) negative used for device

assembly. Second, methods for using thick negative photoresists such as SU-8 with BDPL have been developed which include a new simple and effective method for promoting the adhesion of SU-8 to glass. An assembly method that bonds two individual ultra-thin (<100 μm) replications of the channel and the microfeatures has also been demonstrated. Finally, a pressure driven pumping system with nanoliter per minute flow rate regulation, sub-second response times, and < 3% flow variability has been designed and characterized. The fabrication and assembly of this device is inexpensive and utilizes simple variants of conventional microfluidic fabrication techniques, making it easily accessible to the single cell analysis community.

I dedicate this thesis to my beloved son, Jayden Jacob Myers.

TABLE OF CONTENTS

Page

CHAPTER Page

LIST OF TABLES

LIST OF FIGURES

Figure Page

Figure Page

Chapter 1: Introduction

1.1 Single cell analysis

Single cell analysis methods are finding increasing use for studying disease progression, development, treatment, and prognosis because conventional population based measurement techniques often mask important heterogeneous responses inherent to the disease state. Single cellomics has become increasingly important, especially when investigating highly heterogeneous disease conditions such as cancer; however, these experiments are often difficult and are not compatible with current analyses (Souza, 2011). Conventional techniques for investigating cellular responses lack single cell specificity because the most prominent methods in genomic and proteomic profiling are not sufficiently sensitive to measure single cells. However, genetically homogeneous cell populations exhibit varying degrees of phenotypic heterogeneity that are often the product of microenvironmental cues (Avery, 2006). This phenotypic heterogeneity plays a central role in cell differentiation, proliferation, stimulus response, and carcinogenesis (Zeng et al., 2011). In fact, the responses of individual cells to certain environmental stimuli such as chemotherapeutic drugs varies markedly within a population of cancer cells (Cohen et al., 2008). Studies that probe intercellular variability are therefore critical in understanding how differences in cell phenotype often result in a selective advantage of some cells over others within the same population (Losick & Desplan, 2008). Single cell

studies may also reveal the details behind the decision pathway of the cancer cell phenotype and its ability to evade programmed cell death, or death resulting from an external stimulus such as radiation or drug therapies.

1.1.1 Single cell imaging

Optical imaging modalities allow certain disease phenotypes to be characterized, and provide a simpler, higher throughput platform when compared to conventional molecular biology techniques such as RT-qPCR, gel electrophoresis, or mass spectrometry (Reyzer et al., 2004; Zeng et al., 2011). For instance, microscopic evaluation using hematoxylin and eosin stained sections is the most common method for determining the degree of preneoplastic progression in suspicious lesions (Scheme, 1996). In fact, tissue sections imaged by conventional brightfield microscopy and processed by nuclear morphometry classification algorithms have been demonstrated to correlate with the progression (Pienta & Coffey, 1991) and prognosis (Chapman et al., 2007) of breast cancer. Flow cytometry (FC) has also been used when investigating phenotypical characteristics of human neoplastic disease. For instance, FC was used for characterizing tumorigenicity in various human colorectal cancer stem cell subpopulations (Dalerba et al., 2007). Laser-scanning cytometry offers many of the same features as flow cytometry, but also allows measurements to made over time for studying kinetics and other time resolved processes (Darzynkiewicz, Bedner, Li, Gorczyca, & Melamed, 1999).

A key limitation in current cytometry methods is the loss of information that results from representing 3D objects as 2D slices or projections. Single perspective 2D imaging renders 3D objects incompletely, thus reducing the accuracy of many feature classification protocols. 3D cell imaging is most commonly achieved by confocal laser scanning microscopy (CLSM) in either one-photon (Conchello & Lichtman, 2005) or two-photon (Helmchen & Denk, 2005) configurations. Thin optical sections (focal planes) are acquired from a thick specimen by removing out-of-focus light in each imaging plane, and then reconstructed by computer software into a 3D representation from the stack of images. However, in each case the resolution of the image is non-isotropic (lateral vs. axial resolution are unequal) as defined by the system point spread function (PSF). Two-photon assemblies offer an advance in isotropy over conventional one-photon systems, 1:1.5 vs. 1:3 lateral to axial resolution ratio, however this comes with an increase in hardware costs and practical limitations with most florescent probes. Super-resolution methods have also been developed that exceed the diffraction imposed resolution limit of approximately 200 nm and 600 nm in the lateral and axial directions respectively (Shao, Kner, Rego, & Gustafsson, 2011). However, the use of super-resolution methods is expensive, often requires optimized probes, provides limited temporal resolution, and may not be live cell compatible (Schermelleh, Heintzmann, & Leonhardt, 2010).

A particular method of 3D cell imaging that provides isotropic spatial resolution of 350 nm and the ability to rapidly image isolated individual cells by optical

tomography has been demonstrated (Meyer et al., 2009; Nandakumar, Kelbauskas, Johnson, & Meldrum, 2011). The Cell-CT microscope enables the reconstruction of a set of optical projection images taken at a plurality of perspectives about the cell. In one realization the cell is suspended in a refractive-index matching gel, and rotated in a microcapillary while a piezoelectric-driven, high magnification objective lens scans through the entire cell volume at each of many rotation angles (Fauver et al., 2005). This method has demonstrated the ability to elucidate quantitative differences in cell morphology between esophageal cell lines containing various degrees of dysplasia (Nandakumar et al., 2011), quantify over expressed proteins found in early stages of lung cancer (Miao, Reeves, Patten, & Seibel, 2012), and high sensitivity discrimination of normal vs. metastatic breast cancer cell phenotypes (Nandakumar et al., 2012). However, to date there is no live cell-compatible version of the Cell-CT: The index-matching transport gel the cells are suspended in is not biocompatible. The ability to make this technology live-cell compatible would open up opportunities to study intercellular dynamics. In order to produce a live cell optical projection tomograph, alternative techniques for rotating single cells “free” in an aqueous medium must be investigated.

1.2 Methods for single cell manipulation

Manipulation of single cells in an aqueous growth medium has been studied extensively. The ability to translate single cells has been described by hydrodynamic (Lieu, House, & Schwartz, 2012), optical (Gosse & Croquette, 2002; H. Zhang & Liu, 2008), dielectrophoretic (Cummings & Singh, 2003; Pethig, 2010), magnetic (Gosse & Croquette, 2002), and acoustic methods (Evander et al., 2007). While each of these methods offers the ability to produce a translational force on a cell, only a subset of these methods provide both trapping forces, where the net velocity on the cell is equal to zero, and torsional forces, where forces tangential to the cell boundary produce rotation about an axis through the cell.

1.2.1 Existing techniques for rotating single cells

Rotation of single cells about an axis perpendicular to the imaging plane parallel to the optical axis, denoted as 2D rotation, has been demonstrated by optical (Nieminen, Heckenberg, & Rubinsztein-dunlop, 2001; O'Neil & Padgett, 2002; Paterson et al., 2001), magnetic (Gosse & Croquette, 2002), dielectrophoretic (Voldman, 2006), and hydrodynamic (Shelby & Chiu, 2004; Shelby, Mutch, & Chiu, 2004) methods. These methods have demonstrated the ability to control cell rotation in the medium native to the cell being manipulated. However only, a

limited subset of these techniques has been applied for rotation about an axis parallel to the imaging plane and perpendicular to the optical axis, termed 3D rotation, which is necessary for presenting multiple perspectives of the cell for tomographic cell imaging. The rotation of non-adherent single cells for live cell tomographic imaging has been demonstrated by use of a dielectrophoretic octapole cage (Le Saux et al., 2009). Other freely suspended, single cell 3D rotation methods proposed for applications in single cell tomography (Kreysing et al., 2008), have yet to be demonstrated.

We envisioned an extension of the demonstration by Shelby *et al*. of a 2D microvortical cell rotation device to produce a system for 3D rotation of live single cells. To produce cell rotation about an axis parallel to the imaging plane, the microchamber responsible for producing the recirculating flow profiles must be arranged beneath the main flow channel, as opposed to the previous side-channel configuration (see Chapter 2). As for the 2D cell rotation device, an optical trap is required to hold the cell at the center of the vortex.

1.2.2 Optical tweezers for vortex stabilization

Single beam force radiation-pressure trapping of dielectric particles has been used in many applications involving the micromanipulation single cells (Molloy & Padgett, 2002; Omori, Kobayashi, & Suzuki, 1997; Wright, Sonek, Tadir, & Berns, 1990). The radiation pressure forces that dominate the microscale environment (<1μm), also known as trapping in the Mie regime, have been

predicted through ray tracing and momentum calculations (Nieminen et al., 2001; H. Zhang & Liu, 2008). The trapping capability of single beam optical tweezers can be described by the scattering force and the gradient force. The scattering force is the result of reflection of the incident photons on a dielectric surface as from the mismatch in refractive indices between the particle and the media surrounding it. The scattering force is exerted along the direction of the laser beam, and is maximal when the incident angle of the beam is near normal to the surface of the particle as described by **Equation 1**.The gradient force counteracts the axial component of the scattering force when the particle becomes displaced beyond the point of focus. This is the result of refraction, or the angular change in the light path as it passes through a microparticle with different index of refraction with that of the surrounding media. This change in light path causes a momentum transfer to the microparticle, which experiences a net force towards the direction of the highest electromagnetic gradient as described by **Equation 2**.

$$F_{scatt} = \frac{I_0}{c}\frac{128\pi^5 r^6}{3\lambda^4}\left(\frac{m^2-1}{m^2+2}\right)^2 n_m \qquad \textbf{Equation 1}$$

$$F_{grad} = -\frac{n_m^3 r^3}{2}\left(\frac{m^2-1}{m^2-2}\right)\nabla E^2 \qquad \textbf{Equation 2}$$

I_0 is the intensity of the incident beam, λ is the wavelength of light, m is the index of refraction mismatch, n_m is the refractive index of the surrounding media, r is the radius of the dielectric sphere, E is the electric field, and c the speed of light in a vacuum.

Hence, focused optical beams with a Gaussian profile along the transverse axis, and a parabolic intensity profile along the optical axis, result in the highest electromagnetic gradient at the focal spot. The trapping forces exerted on the microparticle at the focal spot range from 100-2000 pN, which exceeds the forces produced using other microparticle trapping techniques by means of dielectrophoresis, hydrodynamics, magnetics and acoustics (Nilsson, Evander, Hammarström, & Laurell, 2009).

1.3 Fabrication of trapezoidal microfeatures

Fabrication techniques that produce anisotropic microfeatures for microelectromechanical systems have been dominated by wet etching methods (Wu, 1997). However, recent advances in the fabrication of 3D structures have utilized differential exposure of photopolymers to produce various 3D structures. For instance, direct writing of a polymerizable resin by two-photon absorption has been used to create structures with high degrees of anisotropy (Miwa, Juodkazis, Kawakami, Matsuo, & Misawa, 2001). Other demonstrations of anisotropic photopolymer fabrication are the use of gray scale microfabrication (C.M. Waits, Morgan, Kastantin, & Ghodssi, 2005; Christopher M Waits, Modafe, & Ghodssi, 2003) and inclined photolithography (Baek & Song, 2011). However, these fabrication techniques do not offer the ability to produce anisotropic features with an undercut edge, or with an inverse trapezoidal cross-section which prove to be beneficial in producing recirculating flow microvortical

microchambers. However, a particular technique, described as backside diffuser lithography, offered the ability to create undercut 3D features in photoresist (J.-H. Lee, Choi, Lee, & Yoon, 2008). In this thesis, techniques involving anisotropic wet etching of crystalline silicon along its crystallographic planes, and use of backside diffuser lithography were investigated for producing microchambers capable of 3D rotation of single cells.

1.4 Summary of contributions

This thesis research demonstrates the ability to use hydrodynamic microvortices for controlled rotation of single cells about an axis parallel to the imaging plane and perpendicular the optical axis. In Chapter 2, the use of computational fluid dynamics (CFD) is described as a means to investigate important geometric characteristics, such as sidewall angle, microchamber height and microchamber width, and their influences on recirculating flow profiles. In Chapter 3, two methods of fabrication and assembly for producing a 3D microvortical cell rotation are demonstrated. A novel photolithography method was implemented to produce high aspect ratio 3D microstructures in negative photoresist, and new techniques were devised for 3D microfluidic assembly by soft lithography. In addition, a novel, high precision, pulse-free air pressure driven pump, demonstrating nanoliter per minute resolution was designed and developed for cell delivery and controlled rotation of a single cell optically trapped in a

microvortex. The controlled rotation of both 15μm polystyrene beads and single leukemia cells in the 3D microvortex was demonstrated.

Two fabrication and assembly techniques were developed to produce a 3D microvortex chip. The first utilized the anisotropic etching of silicon to produce positive mesa structures which were then compressed against a positive glass channel counterpart to form a mold. The mold was replicated to create a polymer negative, and the device was sealed by bonding a 170 μm microscope coverglass to each side. This approach was augmented with a second, superior method, which used backside diffuser photolithography (BDPL) to produce undercut inverse trapezoids in photoresist on glass to serve as the mold. The process was optimized for SU-8 2035, a thick negative photoresist, and required the development of an adhesion promotion protocol to ensure the microstructures remained intact during processing. The positive SU-8 mold was then used to create ultra-thin (<100μm) trapezoid replications with a coverglass backing, and a main flow channel with a coverglass backing was formed by replicating a laser cut poly(ethylene terephthalate) mold. Finally, the two replicated halves were bonded together to form the 3D microvortex chip.

Lastly, a novel air pressure regulated pump was designed and characterized. The pump allowed for bidirectional flow manipulation at flow rates ranging from 100-1500 nL/min. The absolute time average of variation in the flow rate was 2.6% over two minutes, and the system exhibited an average step response time of 363

ms. The ability to produce constant low particle velocities, and the ability to bring the particle to zero linear velocity in less than a second was demonstrated.

These contributions lay the groundwork for a live cell rotation imaging chamber taking the form of a microscope stage-mounted chip. Together with the precision pump, this chip provides for cell introduction and delivery through a main flow channel, having below it, disposed towards a high-magnification objective lens of the cell imaging system, an optically-addressable trapezoidal microchamber. Individual cells are maneuvered from the main flow channel, through the inlet neck, into the trapezoidal chamber, in which a microvortex is formed by the peeling off of flow streamlines from the bottom surface of the main flow channel. Low, rotational, tangential, fluidic shear forces cause the cell to rotate, its axis stabilized by the optical trap, for multiperspective absorption or fluorescence imaging.

Chapter 2: Design of the optimal microvortex geometry

2.1 Initial 2D microvortex studies

Flow detachment and recirculating flow profiles can be produced by a variety of different microchannel designs; however, a configuration with a microchamber adjacent to a straight flow channel allows for greater versatility when optimizing vertical flow profiles. Lim *et al.* first demonstrated the ability of such a microfluidic configuration to produce microvortical flow in diamond shaped microchambers (Lim, Shelby, Kuo, & Chiu, 2003). The technique was later extended for controlled single cell rotation (Shelby & Chiu, 2004; Shelby et al., 2004). To the author's knowledge, the only three microchamber geometries capable of producing stable recirculating flow in the side chamber configuration at Reynolds numbers less than 10 are the diamond, a derivative of the diamond, termed "fluidic gears", and the rectangle/square (Shen & Floryan, 1985). In an effort to understand which microchamber characteristics created stable recirculating flow for cell rotation, a series of microchamber geometries arranged on the side of a 100-µm-wide channel were designed and fabricated by conventional photolithography and soft lithography methods. Example geometries can be seen in **Figure 1**. It should be noted that while the geometries are to scale, the spacing between features is much greater in the actual mold design.

Figure 1: Examples of microchamber geometries created in a preliminary test chip

To produce the mold, a mask was designed in AutoCAD (Autodesk Inc.) with various microfeature geometries arranged along the side of a flow channel. A 5" chrome-on-quartz mask (Photo sciences Inc.) was used to selectively expose a 60 µm layer of KMPR (Microchem Corp.) on a silicon wafer. The wafer was then developed in MF-26A (Microchem Corp.) and baked at 120 °C to produce a positive hard mold of the feature studded flow channel. To act as a mold release agent, an anti-adhesion silane (tridecafluoro-1,1,2,2-tetrahydrooctyl trichlorosilane; Gelest Inc.), was deposited onto the wafer using vapor deposition. A 10:1 ratio mixture of poly(dimethyl siloxane) (PDMS)(Dow Corning Sylgard 184, K.R. Anderson, Inc.) monomer and cross-linker was then poured over the mold and cured at 60 °C for a minimum of 3 hours before removing the PDMS replica from the mold. Inlet and outlet ports were punched out using a 22-gauge blunt stainless steel needle. Microscope cover glass (25 mm x 25 mm) and the

cast PDMS component were treated with air plasma for 45 seconds at 500 mTorr (PDC-32G, Harrick Plasma) to activate the surfaces prior to direct bonding. The sealed microfluidic device was then placed back into the 60 °C oven for 15 minutes to increase the glass-PDMS bond strength. 18-gauge blunt stainless steel needles were inserted into the inlet and outlet ports to interface with the microchannel. A 1 mL syringe was connected to the inlet port for cell delivery, and for controlling the fluid flow rate during cell rotation.

The full description of the optical trapping setup will be discussed detail in Chapter 4, but briefly a 1064 nm laser is focused through a high numerical aperture objective lens using a custom built non-inverted microscope. Using the optical tweezers, cells are then moved one at a time into a microchamber and stabilized within the microvortex while flow is applied, applying rotation torque to the cell.

For live cell rotation studies cells from an immortalized dysplastic human esophageal epithelial cell line (CP-A) cultured at 37°C and 5% CO_2 atmosphere in Keratinocyte serum-free cell growth medium (Invitrogen, Carlsbad, CA) were trypsinized and loaded into a syringe. Cells were then flowed into and along the microchannel by applying pressure to the input syringe. When a cell of interest approached a microfeature, flow was ceased and the cell trapped using optical tweezers. The cell was then brought into the microfeature and positioned at the

center of the microvortex. Pressure was then applied to the input syringe to create flow in the microchannel, initiating a microvortex and inducing cell rotation.

2.2 Preliminary results obtained from 2D microvortex setup

The microvortex chip described above was used to identify microchamber characteristics that supported recirculating flow profiles suitable for rotating single cells. The cells were trapped using optical tweezers and held in a microchamber while flow was produced in the main channel with a syringe. The first observation made was that microchambers with an incident angle of 90° or greater with respect to the channel were unable to induce cell rotation. In such microfeatures cells were swept away when flow was created in the microchannel, because the lateral forces induced by the flow were greater than the trapping force exerted by the optical tweezers. The circular microchambers on the other hand created smooth and stable rotations proportional to the velocity of fluid in the main channel. Because the circular microchamber designs had the smallest angle of incidence, approximately 30°, it was hypothesized that the incident angle and/or the feature circularity were critical to flow recirculation. Supporting this, stable rotation of a cell was seen in a heptagon shaped microchamber that nearly approximated a circle. Stable rotation was also demonstrated in a trapezoidal shaped microchamber with a back (long) edge parallel to the flow channel. The feature had an incident angle of approximately 56° with respect to the channel.

A critical requirement of the cell rotation device is that it provides interference-free imaging on a plane parallel to the axis of rotation. In this sense, rotation in the trapezoidal microchamber was optimal as it is the only geometry with a flat back surface that can provide high-magnification optical access for such imaging. The other microchamber geometries that enabled stable rotation did not have back edges parallel to the inlet channel, thereby prohibiting interference-free cell imaging. Yet even with a flat back edge, the recirculating flow profile was arranged about an axis perpendicular to the imaging plane, causing the cell to rotate within the imaging plane. For multiple perspective imaging, the cell must rotate through the imaging plane to produce optical sections that are non-redundant. As such, a new design was required to create a recirculating flow about an axis parallel to the focal plane. The use of hydrodynamic vortices for rotating a microparticle or a live cell through the imaging plane was not demonstrated in these preliminary experiments.

2.3 3D microvortex design features

As suggested by the 2D cell rotation study, certain geometrical characteristics were critical for stable rotation of single cells in a microvortex. The 2D microvortex method provided a method for cell rotation in the imaging plane, which served as an effective proof of concept, but was useless for tomography because the long edge of the trapezoid was not accessible by a high-magnification microscope objective. A 3D microvortex was designed to produce recirculating

flows that go through the imaging plane. The critical microfeature parameters that were explored when designing the 3D microvortex chip were the feature inlet width (W_i), feature height (H_f), and incident angle (φ) as seen in **Figure 2.**

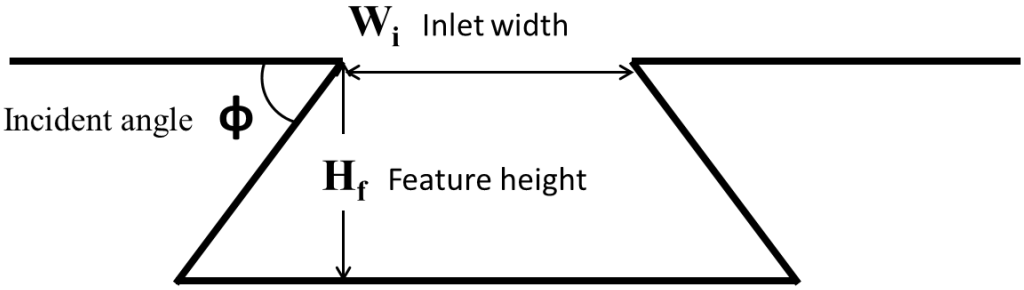

Figure 2: Critical features parameters investigated through modeling

Fluid profiles within side chamber microfeatures were modeled with CFD, to probe the relationship between recirculating flow and microchamber parameters. Models were created using COMSOL Multiphysics v4.2a (COMSOL Inc.), a Finite Element Modeling (FEM) software capable of solving fluid and mass transfer conservation equations.

2.3.1 Recirculating flow profiles in various geometries

Fluid flow in microfluidics is usually in the laminar flow regime due to the magnitude of the effective hydraulic diameter. This often results in cases where inertial effects are negligible compared to the viscous effects (Re<<1), especially

in cases where fluid velocities are low. Under these conditions, the momentum conservation equation (**Equation 3**) for Newtonian fluids of constant density and viscosity can be simplified to the Stokes equation (**Equation 4**) (White, 2006).

$$\frac{\partial \vec{u}}{\partial t} + \left(\vec{u} \cdot \vec{\nabla}\right)\vec{u} = -\vec{\nabla}p + \nu\left(\vec{\nabla} \cdot \vec{\nabla}\right)\vec{u} \qquad \textbf{Equation 3}$$

$$\vec{\nabla}p = \nu\left(\vec{\nabla} \cdot \vec{\nabla}\right)\vec{u} \qquad \textbf{Equation 4}$$

To solve for the velocity field in the microchannel, the flow was assumed to be steady state, incompressible, and laminar. The models made use of the conservation equations for mass and momentum with a defined set of boundary conditions to solve for the velocity field and the pressure across the computational domain. The characteristic geometry included a 100 μm tall channel and various sub-channel microfeature designs defined by the parameters defined in **Figure 2**. The average inlet velocity was defined as 20 μm/s with a parabolic profile and a maximum velocity of 30 μm /s. The outlet condition was defined as having zero pressure and no viscous stresses. The channel top and bottom, along with the boundaries created by the microfeatures, were defined as no-slip walls. Initially, the inlet width and feature height were set to 50 μm and the incident angle was varied from 30°-90°. The results are illustrated as a 2D surface plot of fluid velocity magnitude and an arrow plot of the normalized velocity field (an indication of flow direction) in **Figure 3**. The amount of flow detached from the main channel was directly related to the indent angle of the microchamber

("sidewall angle"). As the angle of incidence increased, the amount of flow contributing to the microvortex decreased. Furthermore, apparent differences in flow circularity were seen across the three geometries. The location of the microvortex center, measured with respect to its displacement from the microchamber inlet, and plotted against various geometric configurations, is shown in **Figure 4**. The incident angles investigated were 30°, 60° and 90° while the microfeature inlet width (W_I) and feature height (H_f) varied from 50 μm to 100 μm. In the graph, the ratio between the W_I and H_f is used to represent the geometric information more effectively.

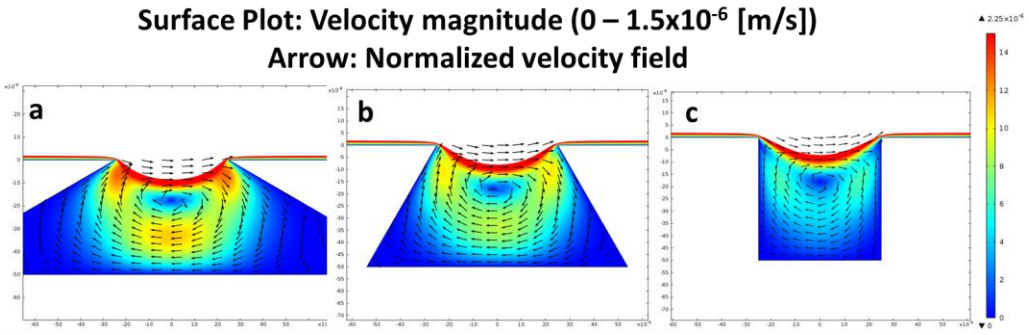

Figure 3: Fluid velocity magnitude and velocity field within microchambers with side wall characteristics. (a-c) 30°, 60°, and 90° incident angles: color scale range 0.0-1.5 μm/s

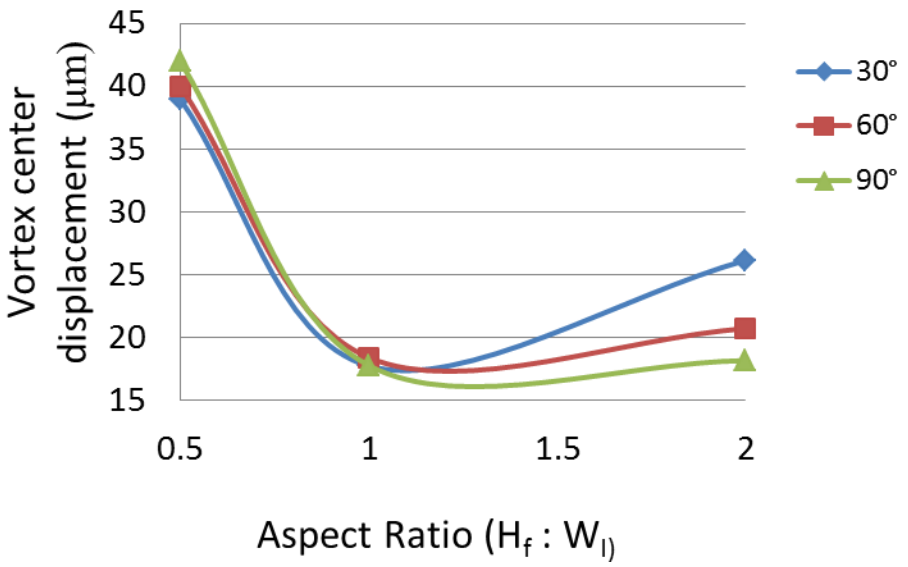

Figure 4: Displacement of the microvortex center from the microchamber inlet

2.3.2 Steady state analysis of a sphere in a microvortex

The initial models demonstrated the ability to create recirculating flows profiles in various microchamber geometries. However, incorporation of a cell-sized circular boundary centered on the microvortex provides a better approximation of the actual flow conditions produced when a cell is rotating in a microvortex. The new boundary produces modified fluid streamlines governed by the boundary condition equations. A no-slip boundary condition is typically used to model non-deformable, immobilized structural interfaces. In this assumption, the fluid velocity at the boundary is assumed to be zero and the boundary shear stress is proportional to the velocity gradient. A generalized model of a rotating outer boundary, similar to that of bulk fluid recirculation which produces rotating

velocity fields on the inner concentric boundary, is depicted in **Figure 5**. This model was used to represent a cell rotating due to forces exerted by rotating velocity fields. The initial conditions state that an outer boundary, r_2 will be set into motion at a constant rotational frequency ω_0 while the velocity field elsewhere is zero. Thereafter, the rotation of the outer boundary causes fluidic shear at r_2, initiating the rotation of the fluid between r_1 and r_2. Because the Reynolds number is so low, the inertial components can be neglected. The viscous shear forces set up a velocity gradient along the r-direction. The solid body surface interacts with the rotating fluid at the boundary of r_1 resulting in a tangential viscous force that initiates the rotation of the solid body. At steady state the rotational frequency, $\omega_{1,}$ of the solid body at r_1 approaches the rotational frequency $\omega_{0\ (=}\omega_{2).}$

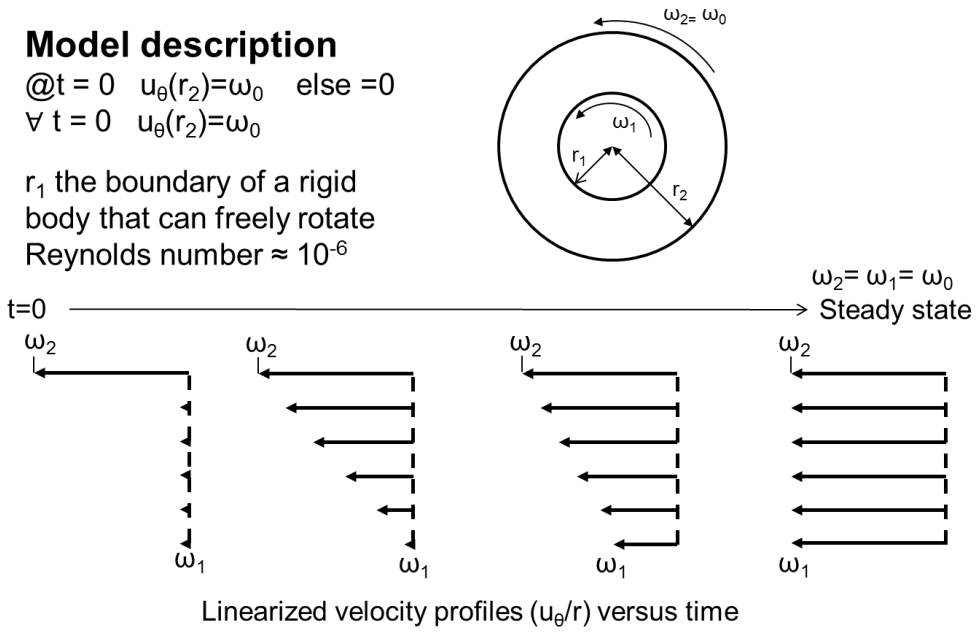

Figure 5: Description of a model of a rotating velocity field inducing rotation of a solid body. The model demonstrates that the steady state angular frequency of the rotating fluid is equal to that of the rotating solid body.

The flow profile within the annulus of two cylinders with radii r_1 and r_2 at constant rotational velocities of ω_1 and ω_2 can be solved for using the cylindrical version of the Navier-Stokes equation (Munson, 1971). Assuming there is no fluid velocity in both r and z and that flow is symmetric about the rotation axis, the resulting continuity equation can be seen in **Equation 5** and its solution after applying the boundary conditions in **Equation 6**.

$$\frac{d}{dr}\left[\frac{1}{r}\cdot\frac{d}{dr}\left(ru_\theta\right)\right]=0 \qquad \textbf{Equation 5}$$

$$u_\theta\left(r\right)=\frac{1}{\left(r_2^2-r_1^2\right)}\left[\left(\omega_2 r_2^2-\omega_1 r_1^2\right)r+\frac{r_1^2 r_2^2\left(\omega_1-\omega_2\right)}{r}\right] \qquad \textbf{Equation 6}$$

When examining this solution, the difference between ω_1 and ω_2 is seen to be proportional to the fluid velocity gradient along r. When the rotational velocities are equal, such as in the steady state condition, the rotational field becomes a linear function of the angular velocity and the r-position. This example can be applied to the case of a rotating microparticle at the center of a recirculating flow profile by assuming the steady state rotational velocity of the cell and the flow surrounding it are equal. However, this case was true only for circular microvortices where velocity gradient is radially symmetric, whereas the microchambers investigated formed oblique-shaped (non-circular) microvortices.

The analytical calculation for an arbitrary flow profile required the use of CFD. We utilized a slip boundary wherein the viscous stresses tangential to the boundary are zero, and the velocity normal to the boundary is zero (no flow across the boundary), to first calculate the tangential velocity imposed on a cell in a microvortex. This essentially prevented fluid from entering the boundary of the cell, but did not prohibit a tangential velocity component on the surface. The tangential velocity magnitude was integrated into a moving wall boundary condition, and then resolved. It was seen that no distinct difference in velocity

field existed between the conditions, indicating that the use of the slip condition approximates the characteristics of a moving spherical boundary in a recirculating flow. While the slip boundary is not a prediction of the physical conditions present in the fluidic system, it can be used to predict the tangential velocity component on a surface, which can then be incorporated into a model that uses conditions, such as rotating walls, to better approximate the actual physical conditions.

Using COMSOL, models of a sphere with a radius of 7.5 μm with a slip boundary condition were placed at the vortex center. All other model conditions remained identical to those in previous studies. The results demonstrating the slip velocity condition for a microchamber with a 60° incident angle can be seen in **Figure 6**. The average velocity about the boundary of the sphere was 2.65×10^{-7} m/s.

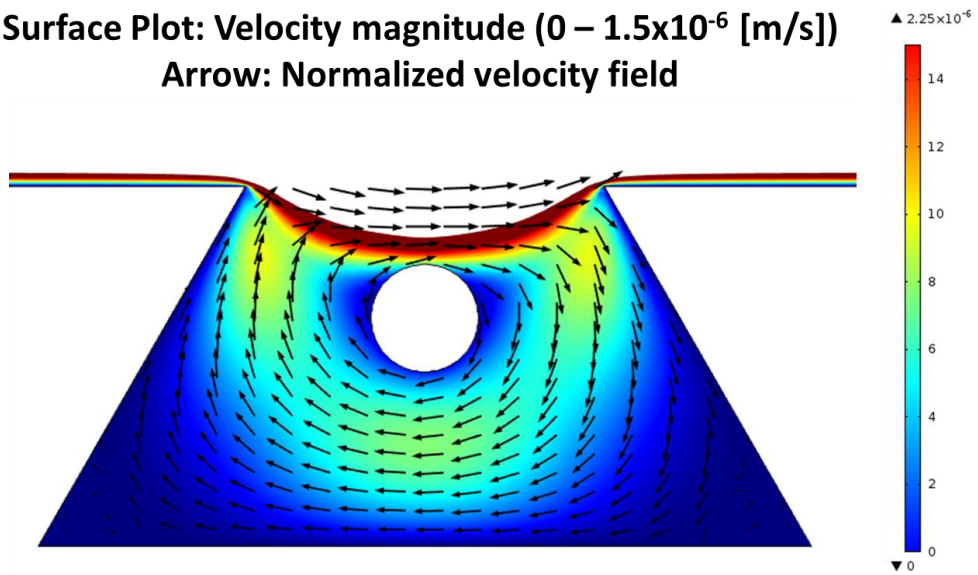

Figure 6: Velocity profile around a 7.5 um sphere arranged at the center of the vortex

To verify the validity of the slip boundary assumption, a moving wall boundary condition with a prescribed tangential velocity equal to the average velocity (22.65×10^{-8} m/s) found using the slip condition was then imposed on a subsequent model. The resulting flow profile was nearly identical to the model that used the slip boundary condition. This demonstrated that the recirculating tangential flow velocity around the boundary of the sphere was approximately the same as the rotational velocity of the sphere as suggested by the model proposed (**Figure 5**).

2.3.3 Effect of microchamber characteristics on rotational velocity and maximum shear rate

The effects of sidewall angle of incidence on the rotational velocity and the maximum shear rate of the sphere were investigated using the conditions described in the previous model. The rotational velocity of the sphere was calculated simply by taking the sphere's average tangential velocity and dividing it by the radius of the sphere. The shear rate is the gradient of the velocity vector and is calculated according to **Equation 7**. The shear rate over the cell surface was then plotted and the maximum value recorded. The maximum shear rate gives an indication of the stability of the microvortex, as a high velocity gradient near the microparticle would destabilize it, causing motion away from the vortex center. If the microparticle moves slightly away from the vortex center, the sudden increase in velocity may eject it from the recirculating flow. This instability was noted in previous demonstrations of microvortical particle rotation (Shelby et al., 2004) and was also seen in our 2D vortex studies (Chapter 2.2).

$$\gamma_{xy} = \frac{\partial u_x}{\partial y} + \frac{\partial u_y}{\partial x} \qquad \textbf{Equation 7}$$

The results as seen in **Figure 7** indicate a strong relationship between the aspect ratio of the microchamber (represented by Λ) and the rotation rate of the sphere. Also notable is that at Λ =1.5, the rotation rate is almost the same, regardless of the incident angle. In addition, there seems to be a strong relationship between the

aspect ratio and the shear rate, where the highest shear rates occur when Λ=1. Changes in the incident angle cause very little change in the shear rate when Λ=1. With Λ=2, however, the difference in incident angle changes the shear rate substantially.

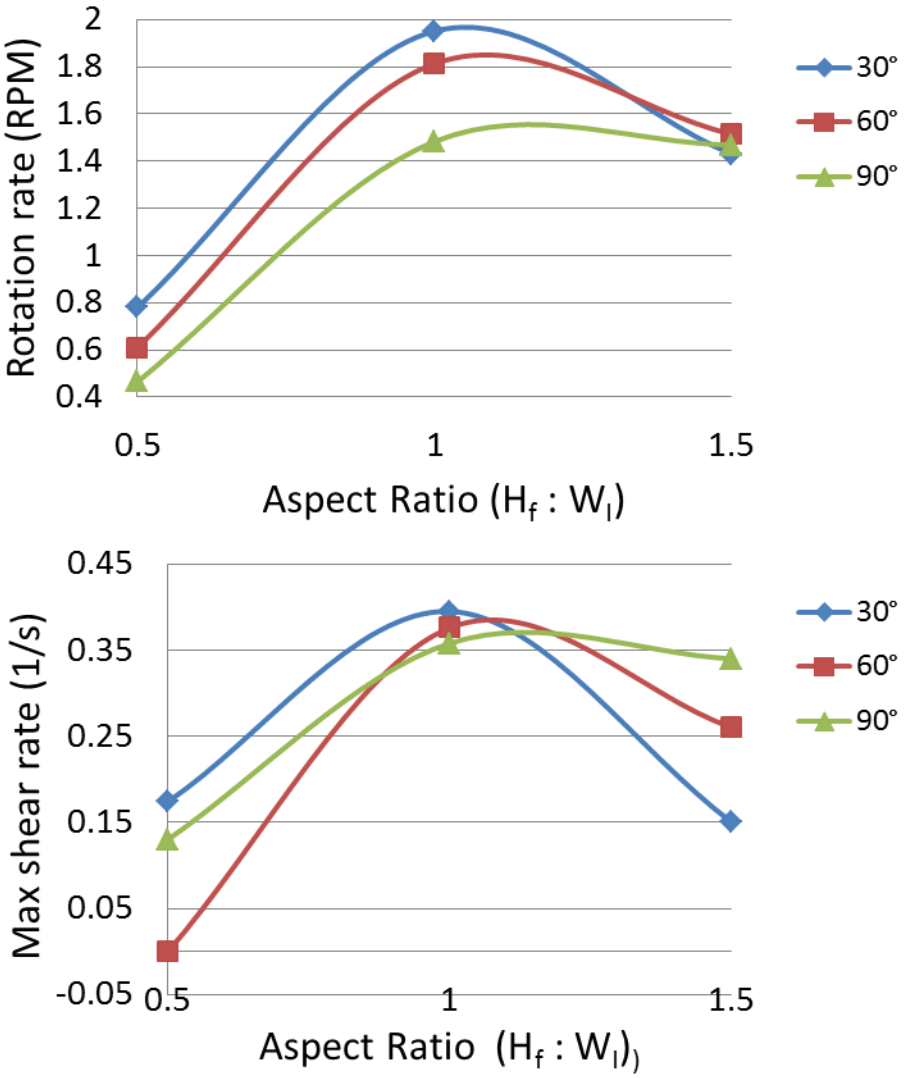

Figure 7: Rotational velocity and maximum shear rate for microchambers with various incident angles and aspect ratios

2.3.4 Discussion of modeling results

COMSOL Multiphysics was used to perform computational fluid dynamics to determine the critical dimensions for producing stable recirculating flow profiles. The initial models analyzed the steady state flow profiles in various trapezoidal shaped microfeatures. It was seen that the features with lower incident angles peeled off a greater portion of flow from the main channel, creating stronger microvortices. Greater displacement of the vortex center with respect to the channel inlet is favorable, as the cell is less susceptible to the high velocity streams near the channel inlet. Additionally, in a 3D vortex system, the distance between the cell and the imaging objective would be reduced at smaller sidewall angles, which is optimal when using objective lenses with limited working distances. Having a cell closer to the long side of the trapezoid also prevents clipping of high angle light rays of the optical tweezers by the back corners of the microchamber at the channel inlet. Conversely, if a bottom facing objective were used for optical trapping, beam clipping problems would occur if the vortex center were too deep in the microchamber (discussed in Chapter 4). However, the position of the vortex center when $\Lambda=2$ is highly controlled by the incident angle, which could be utilized to tune its position if an optical limitation arises.

To study flow characteristics at the boundary of the sphere, a steady state approximation of fluid interactions with a spherical boundary was used. Once again, the results of modeling with $\Lambda=2$ shows that the incident angle controls the

shear rate. The farther the vortex is from the main flow in the channel, the lower the shear rate exerted on the cell. In any case, the rotational rate at $\Lambda=2$ is nearly identical for all incident angles. In conclusion, the microchamber geometry that produced the lowest shear rate with a high rotation rate is that with a feature height of 100 µm, an inlet width of 50 µm and a sidewall angle of 30° incident to the flow channel.

Chapter 3: Fabrication and assembly

The results from the 2D microvortex experiments and the CFD modeling show that trapezoidal features are appealing for 3D microvortical cell rotation. Trapezoidal features provide a sharp inlet corner that effectively peels off fluidic streamlines from the main flow channel into the microfeature, inducing recirculating flow profiles. In addition, trapezoids provide an optically flat edge for distortion-free optical access for high magnification imaging. However, directly microfabricating undercut features is uncommon and typically avoided when using conventional microfabrication techniques. As an example, advances in high-resolution fabrication methods common to the semiconductor industry often focus on creating high aspect ratio features with 90° sidewalls.

3.1 Microfeature and channel mask design

The results from the preliminary experiments indicated that cell rotation can be produced with a variety of microchamber geometries. To use the microfabrication methods described in the following sections, a new mask design that allowed for the fabrication of various geometries, including undercut geometries, was required. Since 3D microfeatures, features not confined to the x-y plane, were now being fabricated, the mask features dictated the inlet width and the length of the microchamber. The length was set to 2.54 mm in the main design and the feature inlet size ranged from 20 μm to 150 μm. A set of alignment marks were included to aid in device assembly. In a second design, the features were designed

to incorporate optical fibers for trapping, and required larger dimensions. In this design the feature length was 32 mm and the widths varied from 50 μm to 260 μm. Finally, a mask was designed for the main flow channel. The footprint was designed to fit a standard 25 mm x 75 mm microscope slide format; therefore the length of the channel was set to 70 mm. The main flow channel also incorporated two different expansions. The first is the observation portion of the channel (width of 3 mm), which places the microfeatures within the channel when properly aligned. The second expansion was incorporated for cell extraction following rotation. The mask designs for the microfeatures and for the main flow channel can be seen in **Figure 8**.

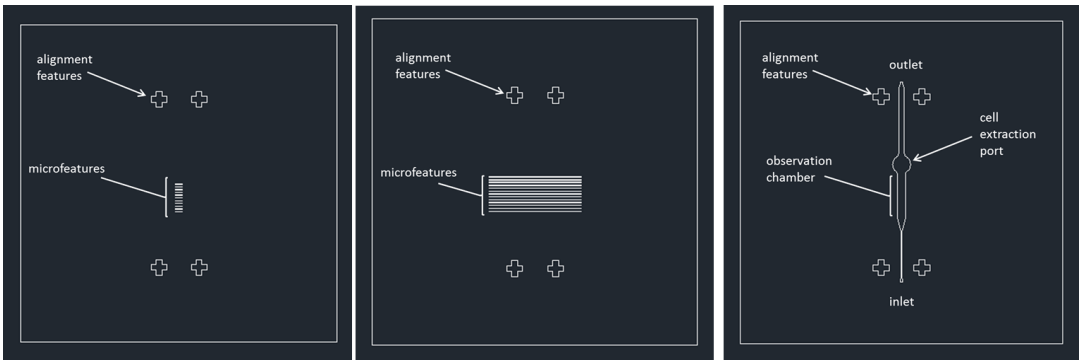

Figure 8: Mask designs (left) main microfeature mask (middle) microfeature mask for optical fiber integration (right) main flow channel mask

3.2 Anisotropic etching of silicon

Production of anisotropic structures is most commonly achieved by wet etching of crystalline silicon in an alkaline solution. When conditions are properly

controlled, this fabrication technique can reliably produce structures with trapezoidal cross sections. The angles are formed because the etching process terminates at the crystallographic planes (<110>, <100>, etc. planes) of crystalline silicon, producing angles equivalent to the various plane orientations. The features produced directly by this method are obtuse with respect to the substrate plane (Figure 9, steps 8 and 9). The etching process requires temperature, concentration, and agitation to be optimized in order to minimize processing time and maximize device functionality (feature perfection). All of the following fabrication steps were conducted in a class-100 cleanroom at the ASU Center for Solid State Electronics Research (CSSER). **Figure 9** depicts the overall fabrication process for the fabrication of silicon anisotropic mesas that was utilized in this research (acronyms are explained in the following paragraph).

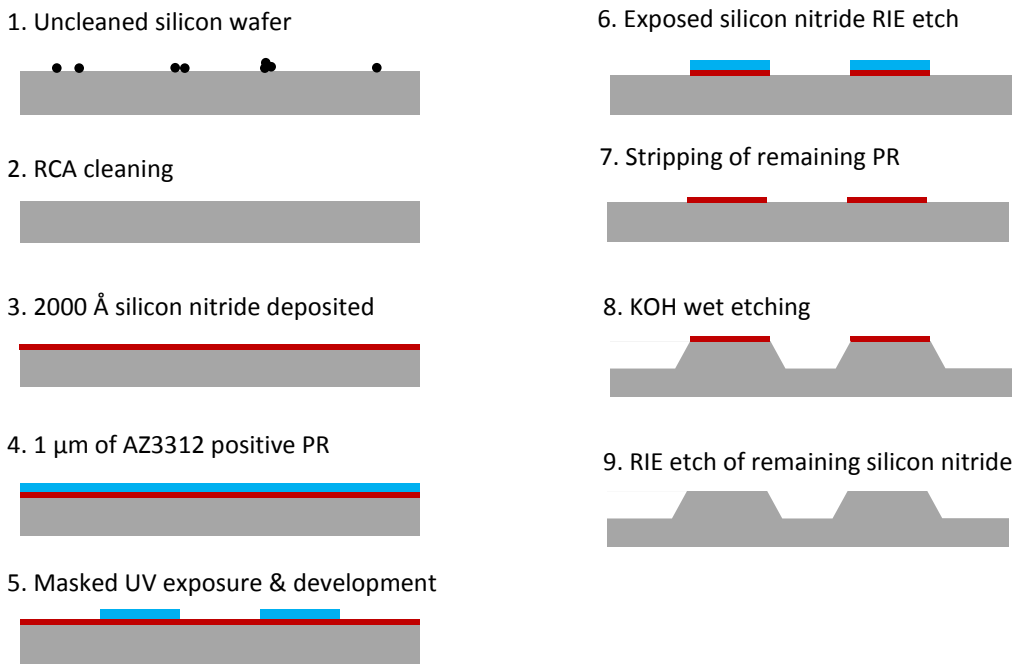

Figure 9: Process flow for anisotropic etching of silicon

Four-inch positive (p)-type silicon wafers with a <100> crystal orientation were cleaned with the standard three-step RCA cleaning protocol common in semiconductor manufacturing. First, organic contaminants were removed by immersing the silicon wafers in a solution of de-ionized (DI) water, ammonium hydroxide, and hydrogen peroxide at a 5:1:1 ratio heated to 75°C for 15 minutes, and then rinsed in a DI water bath. Next, the oxide layer formed in the previous step was removed by immersing the wafers in a 20:1 solution of water and hydrofluoric acid at room temperature for one minute, followed by washing in a DI water bath. The wafers were then immersed into a 75°C solution of DI water, hydrochloric acid, and hydrogen peroxide at a ratio of 6:1:1 for 15 minutes to remove metallic contaminants. Finally, the wafers were soaked in a DI water bath

for five minutes, dried with N_2 gas, and baked at 100°C for 30 minutes. To act as a mask for the wet etching procedure, a 2000 Å silicon nitride (Si_3N_4) layer was deposited using plasma-enhanced chemical vapor deposition (Oxford Plasma Lab 100 PECVD). Following that, 1 µm coating of AZ 3312 positive photoresist ("PR" in Figure 9; AZ Electronic Materials USA Corp.) was spun onto the wafers with a precision spin coater (Specialty Coating Systems, P-6708) at 3500 RPM for 30 seconds. The photoresist was then soft-baked at 90 °C for 60 seconds. The wafers were then exposed to 45-50 mJ/cm^2 (6-8 seconds, OAI 808 Aligner) through a transparency mask (**Figure 8**) (Fine Line Imaging), developed in AZ 300MIF (AZ Electronic Materials USA Corp.) for 3 minutes, and hard baked at 110 °C for 60 seconds. Subsequently, the exposed nitride mask was removed by Reactive Ion Etching (RIE) (Plasmalab M80 Plus RIE) in an environment of CHF_3 and O_2 gases (using the parameters shown in **Table 1**).

Table 1 : Silicon Nitride RIE recipe

Process Characteristic	**Values**
Pressure	50 [mTorr]
Power	150 [Watts]
CHF_3 gas flow rate	50 [sccm]
O_2 gas flow rate	5 [sccm]
Time	17 [minutes]

The remaining photoresist was stripped by immersing the wafers in a 100 °C solution of Microstrip 2001 (FujiFilm USA) for 5 minutes, and then rinsed

thoroughly with DI water and dried with N_2 gas. The wafers that were used in the design of experiment procedures described in the following section were diced into 20 individual 13 mm x 20 mm test chips using a diamond saw (Micro Automation M-1006A). The masked silicon wafer was then etched with potassium hydroxide (KOH), as described in the following sections.

3.2.1 Design of experiment response variables, factors, and levels

The chemical etching of the masked silicon was the most critical processing step, as large defects such as pocketing and chipping can occur with incorrect etching conditions. Also, the etch time can vary from several minutes to several hours for a process that has not been optimized. To improve this chemical etching process a three factor full factorial design of experiment (DOE) was conducted. In order to quantify the optimum etch conditions, two response variables were investigated: surface roughness and etch rate. The surface roughness should be minimized to avoid unwanted defects in the microfeatures, and to create a smooth surface that will later be used as a mold. Etch rate, on the other hand, should be maximized to reduce processing and fabrication times. The factors controlled in the experiment were KOH concentration, etchant temperature, and agitation method, where the concentration and temperature are quantitative factors and the agitation method is a qualitative factor. There are numerous reports that demonstrate the effects of KOH concentration and temperature on etch rate and surface quality (Palik, Glembocki, Heard, Burno, & Tenerz, 1991; Sat et al., 1998; Shikida, Sato,

Tokoro, & Uchikawa, 2000), while only a few have reported on how agitation affects these characteristics (Park et al., 2008; Yang, Chen, Chiou, & Lee, 2005). To optimize the etching conditions, a completely randomized, full-factorial design was used to extract maximal information from the experiment. The levels chosen for KOH concentration were 20, 30, and 40% by weight (in water). These values were selected for two main reasons. First, the stock concentration of the KOH was 49% by weight, limiting the use of higher concentrations; and second, lower concentrations were not selected because low etch rates would have been difficult to quantify with a contact profilometry instrument, as the measurement resolution decreases drastically when features approach sub-micron geometries. The temperature levels chosen were 25, 45, and 65 °C. A temperature above 65 °C was not desirable since etching conditions become more hazardous as temperatures approach the boiling point of the KOH solution. Temperatures below room temperature were not appropriate for this experiment, as the etch rate is too slow to be practical. Ultrasonic agitation and magnetic stirring were investigated as agitation methods.

Other factors held constant in the experiment include crystalline orientation and type of the silicon wafers (<100>, 4" p-type), pre-processing materials and processes (batch of photoresist, recipes for photolithography and RIE), 60-minute etch time, and the instruments used for processing and measuring. In addition, center points were included in the experimental design to verify if a curve-linear relationship between the chosen factors is present, and to distinguish run-to-run

variations. The factors, levels, and center points are presented in the 3D graph of **Figure 10**.

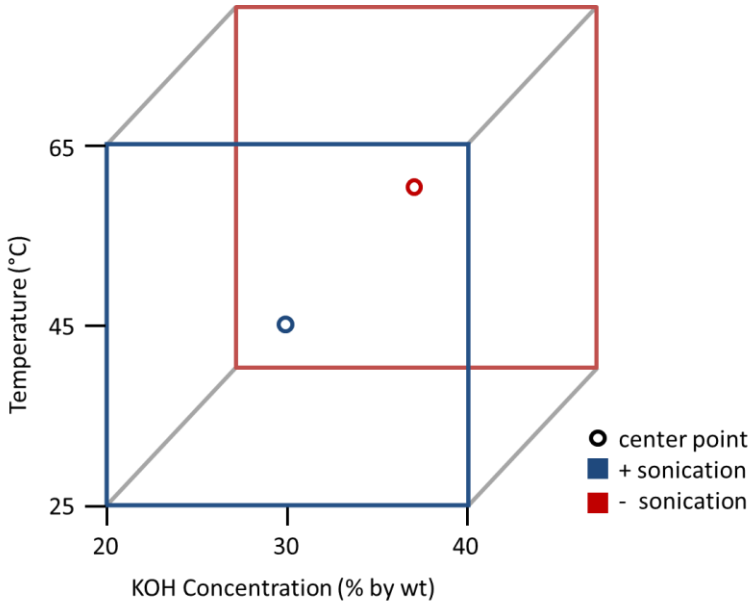

Figure 10: Design of experiment space for silicon etch process

3.2.2 KOH etching experimental setup

Two different experimental setups for conducting the KOH etching experiments were used: The first utilized a hotplate with a magnetic stirrer, while the second employed a heated ultrasonic bath as shown in **Figure 11**. The hotplate configuration used a water bath to raise the temperature of a small beaker filled with KOH solution and containing a magnetic stir bar. The etching solution was heated for 20 minutes prior to adding the silicon chip in order to ensure the etchant solution was at the same temperature as the water bath, as measured by a thermometer. After preheating, a small Teflon chip holder containing the silicon

chip was placed in the beaker. For optimal mixing, the holder was arranged with the silicon chips suspended above the magnetic stir bar. All chips were exposed to the etchant for 60 minutes. Immediately after etching, the Teflon holder and silicon chips were placed in a bath of 70% isopropanol and stirred for 5 minutes to terminate the etching reaction, then washed with DI water.

Figure 11: KOH etching experimental setup. Left panel: Hotplate, with magnetic stirring. Right panel: Heated ultrasonic bath.

The ultrasonic bath configuration was nearly identical to the hot plate setup, but the bath had a built-in heater and temperature probe to control the temperature. In addition, the Teflon holder was not necessary, as the ultrasound agitation is nearly isotropic, so the chips were placed mask side up in the bottom of a small beaker containing the preheated etchant.

3.2.3 KOH etching response measurement

Etch rate and surface roughness were measured by a Dektak 150 Stylus Profiler (Veeco Instruments Inc.). Prior to etching, samples from each wafer were profiled to get baseline values. A 2D profile of a 100-µm-wide silicon nitride feature was measured to get the initial mask height, for use in the calculation of etch rate. This profiling process was then repeated at the same location on each of the etched samples. An example profile can be seen in **Figure 12** where the x- and y-axis are in units of micrometers. The profile seen is a profile of the silicon nitride mask prior to the etching process.

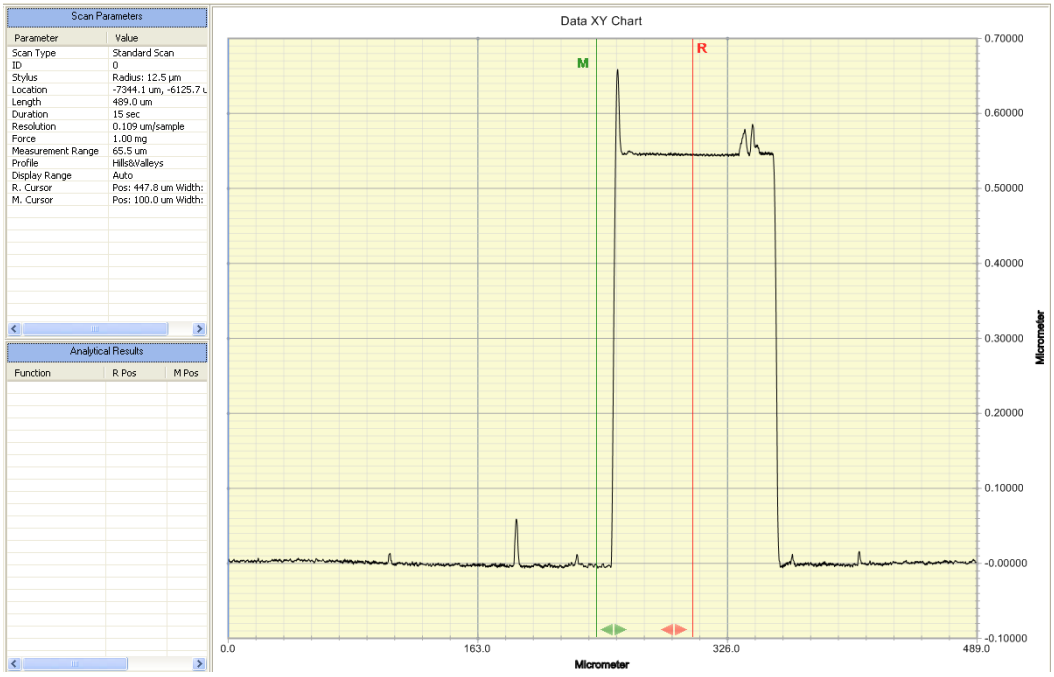

Figure 12: Example stylus profilometry measurement results (x- and y-axis in units of micrometers)

The depth of the feature was obtained by measuring the difference between the baseline mask height, and the peak height of the microfeature after etching. The etch rate calculation is given by **Equation 8**

$$\frac{dz}{dt} = \frac{z_{\max} - z_0}{t}$$

Equation 8

where z_{max} is the peak of the microfeature, z_0 is the initial mask height measurement, and t is time of the etch (60 minutes). The surface roughness measurement was obtained by measuring the fluctuation in the surface height across the surface adjacent to the microfeature edge. The surface roughness is calculated by the instrument and is the arithmetic average deviation from the mean line within the assessment length. The expression for surface roughness is defined by the American National Standards Institute's B46.1 specification according to **Equation 9**

$$R_a = \frac{1}{L}\int_{x=0}^{x=L} | z | dx$$

Equation 9

where L is the assessment length, z is the difference in height deviation from the mean line, and x is the position along the length of the profile. Etch rate determination and surface roughness calculations were compared among processes at various points in the DOE space to determine the optimal processing characteristics.

3.3 Silicon sandwich assembly

In order to create a trapezoidal side chamber, a negative polymer casting method was investigated. Because of the intrinsic limitations of this anisotropic etching process, the angle formed between the trapezoid and the substrate of the wafer is inherently obtuse. As a result, as shown in **Figure 13**, conventional direct replication techniques cannot be used, as the microfeature requires an acute edge with respect to the flow channel to produce a stable recirculating flow within the microfeature. To resolve this limitation, a modified replication and assembly procedure, dubbed the "silicon sandwich assembly," was developed so that an acute (undercut) microfeature edge could be formed.

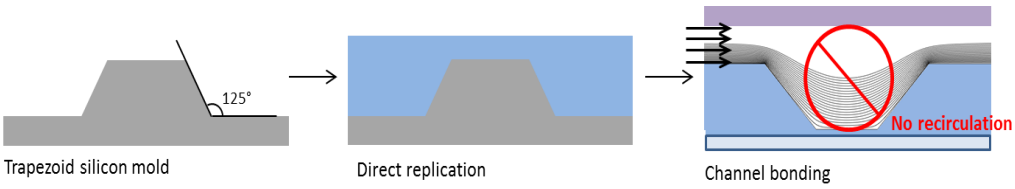

Figure 13: Unsuitability of direct replication for silicon trapezoidal microfeatures

The silicon sandwich assembly method requires two microfabricated wafers to be compressed together forming a two-part mold. One half of the mold is a silicon wafer containing anisotropically etched microfeatures with oblique sidewalls, while the other half is a 500-µm-thick borosilicate glass wafer (Borofloat 33) containing a positive feature in the shape of a channel. The positive microchannel

is created by cutting the main flow geometry seen in **Figure 8 (**right panel) out of a piece of high tack semiconductor dicing tape (Semiconductor Equipment) with a CO_2 laser system (Universal Laser Systems XL-9200) and adhering it to the silicon dioxide wafer. The dicing tape acts as a mask for a wet etch process, in which the entire wafer aside from the channel mask will be etched away. The wafer is isotropically etched in a 49% hydrofluoric acid solution for 10 minutes, yielding a channel thickness of approximately 100 μm.

The two halves of the mold are then coated with a monolayer of PDMS by a surface modification protocol described previously (M. J. Lee et al., 2006). Through this anti-adhesion protocol, unconventional materials can be used for the soft lithographic replication. Specifically, photocurable adhesives can be used to efficiently create durable prototypes, advantageous due to their increased mechanical strength and shorter cure times. The surface passivation protocol and chemistry are shown in **Figure 14**. First, the silicon mold is dehydrated at 160 °C for 30 minutes to remove any moisture on the wafer surface. The silicon surface is then oxidized under air plasma at 500 mTorr for 45 seconds and then immersed for 30 minutes in a 60 °C bath of amine-terminated silane (3-(aminopropyl triethoxysilane) (APTES) (Gelest Inc.) at 0.5% by weight in methanol. The concentration of 0.5% APTES was selected because the maximum concentration that allows monolayer coverage without physisorption is 0.4% in an anhydrous solution (Uvdal, Erlandsson, & Elwing, 1991); however the solvent used in this method was not dehydrated prior to use for reasons of practicality. Therefore the

marginal concentration increase was chosen in order to compensate for the condensation reactions that could occur between the APTES and the residual water in the methanol solution. The concentration adjustment was an approximation and its effects were not characterized experimentally. Following APTES deposition, the silicon mold is baked at 160 °C for 20 minutes to promote siloxane polymerization (Kim, Seidler, Wan, & Fill, 2009). The aminosilane-grafted mold is then reacted with a monoglycidyl ether terminated PDMS (MET-PDMS) (Gelest Inc.) for 4 hours at 80°C, causing an epoxy-amine conjugation. Following conjugation, the wafer is washed in isopropyl alcohol (IPA) three times and dried with N_2 gas to remove any unbound silane.

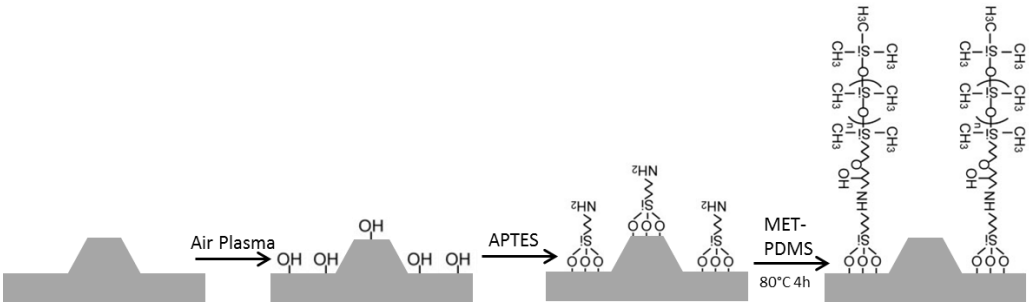

Figure 14: Mold release surface modification process

After the mold components have been modified to prevent the adhesion of the photocurable polymer, the two surface-modified mold components are roughly aligned and held together with fold over clips to create a space 150 μm thick where the two surfaces of the positive molds are not in contact as shown in **Figure 15**.

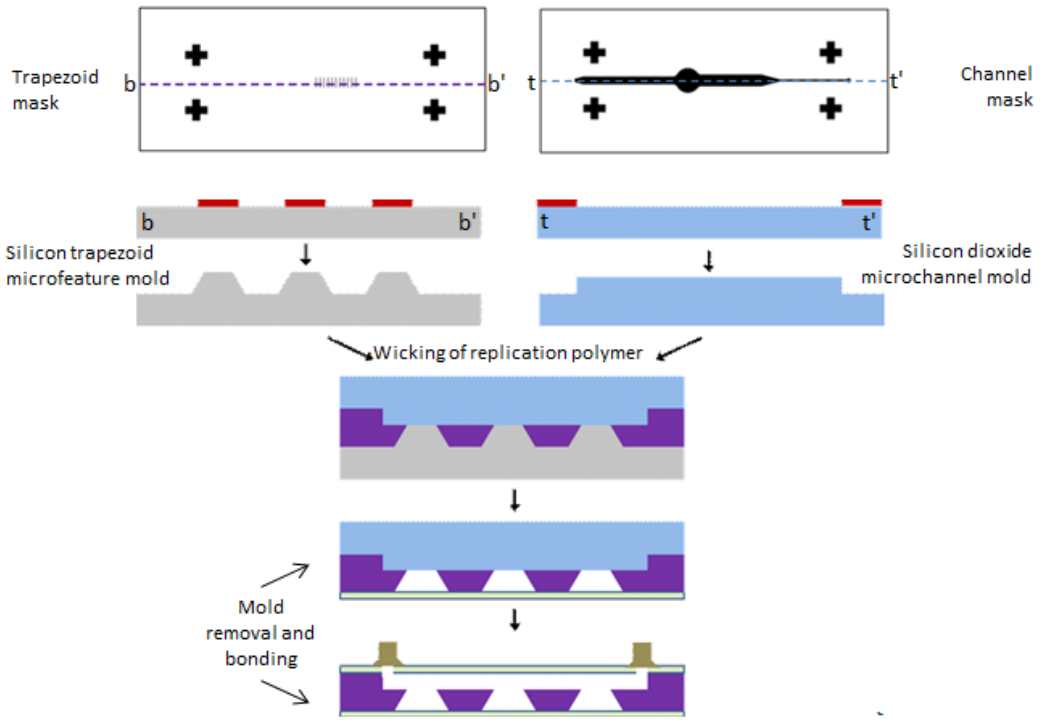

Figure 15: Fabrication and assembly process flow for the "silicon sandwich" method

A urethane-based UV-curable polymer (Norlands Adhesive 81), generally used as an optical adhesive, was used as a soft lithography material. The adhesive was wicked between the two mold halves by capillary action and exposed to UV light

for 1 minute. The silicon mold was then carefully removed to expose the surface containing the back face of the trapezoid. A 50 mm x 75 mm x 0.170 mm microscope cover glass (Ted Pella Inc.) that had been oxidized in air plasma (500 mTorr, 45 seconds) was then bonded to the polymer surface by means of direct bonding. The bond strength was increased by placing the mold assembly into a 60 °C oven for 5 minutes. Following this, the silicon dioxide mold was carefully removed from the polymer-glass assembly, exposing the top surface of the microchannel. A 0.5 mm thick borosilicate glass wafer was diced to 50 mm x 75 mm x 0.5 mm with a diamond bit saw. Two 350 μm diameter circles were then cut out with a high-powered 355 nm laser (Coherent AVIA). Finally, the machined glass was oxidized in air plasma (500 mTorr, 45 seconds), aligned over the extent of the microchannel, and bonded to the polymer surface by direct bonding. A schematic of the assembly process is shown in **Figure 15**. Again, the entire assembly was placed into a 60 °C oven for 30 minutes to ensure proper bonding. Fluidic connections (Upchurch Scientific, N333 Nanoport) were adhered over the inlet and outlet ports to allow for cell delivery.

3.4 Backside diffuser photolithography

An innovative alternative method to fabricate trapezoidal microfeatures is backside diffuser photolithography (BDPL). BDPL incorporates traditional backside photolithography with a novel integration of an optical diffuser. This method allows various polymeric 3D microfeatures to be created with trapezoidal

and elliptical cross sectional geometries (J.-H. Lee et al., 2008). Feature characteristics such as sidewall angle are controllable, unlike in anisotropic etching of silicon, in which case angles are constrained to the crystal lattice plane orientations in the material. With backside exposure, undercut features can be easily made, permitting the use of direct replication techniques.

To fabricate the backside mask, the BDPL process began by vapor depositing 100 nm of chromium onto a RCA cleaned (process described in 3.1) 4" borosilicate glass wafer (CHA E-beam Evaporator). A 1 μm thick layer of AZ 3312 positive photoresist (AZ Electronic Materials USA Corp.) was spun onto the wafer at 3500 rpm for 30 seconds using a precision spin coater. The wafer was then soft baked on a hot plate for 1 minute at 100 °C and exposed to 45-50 mJ/cm^2 (6-8 sec) through a transparency mask (**Figure 8**). The patterned photoresist layer was then developed in AZ 300MIF developer and baked at 110 °C for 1 minute to evaporate off residual solvent. The patterned photoresist wafer was then immersed for 60 seconds in a chrome etchant solution (Transcene Inc.) containing a mixture of 6% nitric acid and 16% ceric ammonium nitrate in water. The wafer was then immersed in a bath of DI water for 5 minutes and dried with nitrogen gas. By this process, the chrome that was not masked by photoresist was removed, resulting in a glass mask having an embedded chrome pattern required for backside photolithography. Finally, the AZ 3312 photoresist was removed by immersing the wafer in a 100 °C solution of Microstrip 2001 for 5 minutes.

After the embedded chrome mask was patterned onto the wafer, an adhesion promoting silanization procedure was performed. First, the wafer was dehydrated at 160 °C for 30 minutes to remove any moisture on the wafer surface. The wafer surface was then oxidized in air plasma, and immersed for 30 minutes in a 60 °C bath containing 3-(aminopropyl triethoxysilane) (APTES) at 1 percent by weight in methanol. The wafer was cured for 20 minutes at 160 °C. A 5 μm layer of SU-8 2005 was then spun onto the wafer using a precision spin coater at 6000 RPM. Following spin coating, the wafer was baked for 1 minute at 65°C and 2 minutes at 95°C on a hotplate, and then exposed to 135 mJ/cm^2 (14 seconds). The wafer was then hard baked at 95°C for 30 minutes. Thereafter, a 50 μm layer of SU-8 2035 (Microchem Corp.) was spun at onto the wafer using a precision spin coater at 2000 RPM. The wafer then was soft baked according to the recipe described in **Table 2**.

Table 2: SU-8 soft bake recipe

Thermal Cycling Stage	Temperature (°C)	Time (minutes)
1	Ramp from 20 °C to 65 °C	Approximately 5 min
2	Hold at 65 °C	30 min
3	Ramp from 65 °C to 95 °C	Approximately 5 min
4	Hold at 95 °C	3 minutes
5	Cool at 20 °C (remove from hotplate)	5 minutes

After the wafer cooled to room temperature, it was positioned photoresist side down on top of a plain glass wafer. The assembly was then placed onto the wafer chuck of the exposure tool so that the backside of the chrome patterned wafer faced towards the UV lamp as seen in **Figure 16**. Approximately 250 µL of water was then deposited on the backside of the wafer as an index matching liquid (IML; green in **Figure 16**) to optically couple the wafer to the diffuser. The wafer and a 5" square opal diffuser (NT02-149, Edmund Optics Co) were brought into contact, spreading the water across the entire wafer. Finally, an i-line long pass filter was placed on top of the diffuser to provide optimal photoresist exposure (PL-360LP, Omega Optical).

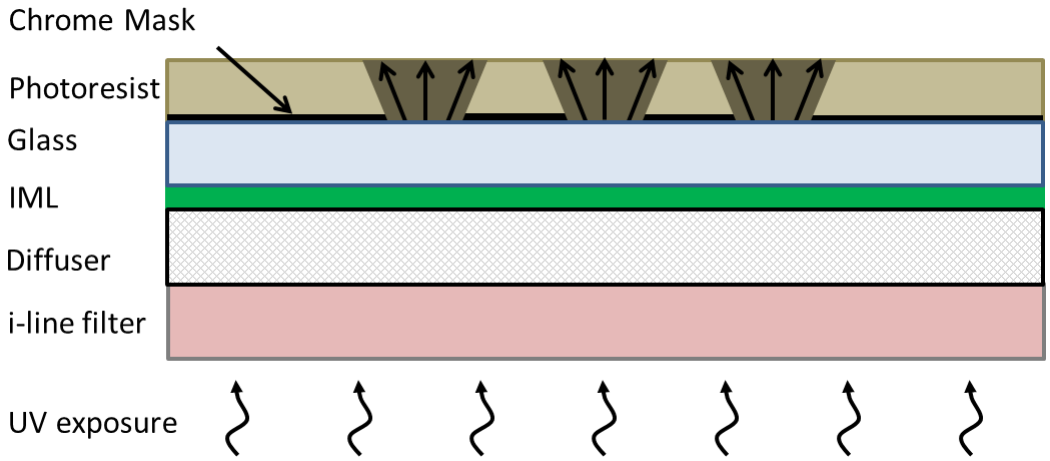

Figure 16: Backside diffuser photolithography exposure assembly

The wafer is exposed to 575 mJ/cm^2 (60 seconds), removed from the assembly, and post- exposure baked according to the recipe described in **Table 3**. The longer dosage at 65 °C helps to reduce stresses introduced by evaporating off the solvent

at higher temperatures. The longer dose at both high and low temperature stages also serve to reduce the total solvent content, helping to crosslink the exposed photoresist to the substrate. Following the baking process, the photoresist is developed for 15 minutes in SU-8 developer (1-Methoxy-2-propanol acetate, Microchem Corp), washed with isopropanol, and dried with N_2 gas. Finally, the wafer is hard baked at 160 °C to remove any residual solvent from the photoresist.

Table 3: SU-8 post exposure bake recipe

Thermal Cycling Stage	Temperature (°C)	Time (minutes)
1	Ramp from 20 °C to 65 °C	Approximately 5 min
2	Hold at 65 °C	60 min
3	Ramp from 65 °C to 95 °C	Approximately 5 min
4	Hold at 95 °C	6 minutes
5	Hold at 20 °C (remove from hotplate)	5 minutes

3.5 Stacked multi-layer assembly

The product of BDPL is an array of positive SU-8 microfeatures that can directly act as a mold for a soft lithography process. To ease mold delamination, the surface was treated with an anti-adhesion silane. The mold surface was first oxidized in air plasma for 45 seconds at 500 mTorr. After surface oxidation, tridecafluoro-1,1,2,2-tetrahydrooctyl trichlorosilane was deposited onto the wafer

surface by vapor deposition. Then a 10:1 ratio of PDMS-to-crosslinker mixture was poured over the mold and placed into a desiccation chamber under vacuum for 30 minutes to release any bubbles cavitated in the trapezoid microfeatures. A 75 mm x 50 mm piece of 170 µm-thick microscope cover glass (Ted Pella Inc.) was oxidized in air plasma (500 mTorr, 45 seconds) and placed on top of the PDMS. A 500 g weight was then set on top of the glass to displace any excess PDMS from beneath the glass. After the excess was extruded, the total thickness of the PDMS layer was reduced to match the thickness of the mold. The PDMS-glass assembly was then cured at 60 °C for a minimum of 3 hours before removing the polymer replica from the mold.

A similar replication procedure was applied to mold a microchannel that constitutes the top half of the microfluidic device. In contrast to the trapezoidal microchambers, the characteristic features of the microchannel do not depend on specific sidewall angles or sharp feature edges. Since micron-scale resolution is not required, the microchannel mold can be fabricated by simpler techniques. A method similar to that described by Luo *et al.* was used to fabricate flexible channel molds with 75 µm resolution and turnaround times of just a few hours (Luo et al., 2007). First, a positive mold was fabricated by laser cutting 100-µm-thick pieces of an adhesive film (2 mil Melinex with adhesive on 2 sides, Fralock Materials) into the shape of the microchannel. These pieces were adhered to a 250-µm-thick polyester film (10 mil Melinex, Fralock Materials). A 10:1 ratio of PDMS to crosslinker mixture was then poured over the positive feature. Again, a

75 mm x 50 mm piece of 170-µm-thick microscope cover glass treated in air plasma was placed on top of the PDMS and loaded with a 500 g weight prior to curing at 60°C. After removing the PDMS-glass component from the mold, inlet and outlet ports were laser cut (Coherent AVIA) at the ends of the channel by the process described in Chapter 3.2.

After forming the two device halves —the trapezoidal PDMS replication and the PDMS-cover glass channel— the device was assembled by direct bonding. Both PDMS surfaces were oxidized in air plasma (500 mTorr, 45 seconds) forming siloxy groups on the surface. These siloxy groups react readily with each other when close contact is achieved, forming a strong bond between the two components. While still separate, the two halves are aligned so that the lateral channel covers the extent of the microfeatures, and then they are brought into contact. Immediately following adhesion, the device is annealed at 60°C for 20 minutes. Finally fluidic ports are attached at the channel inlet and outlet. The multilayer assembly process is depicted in **Figure 17**.

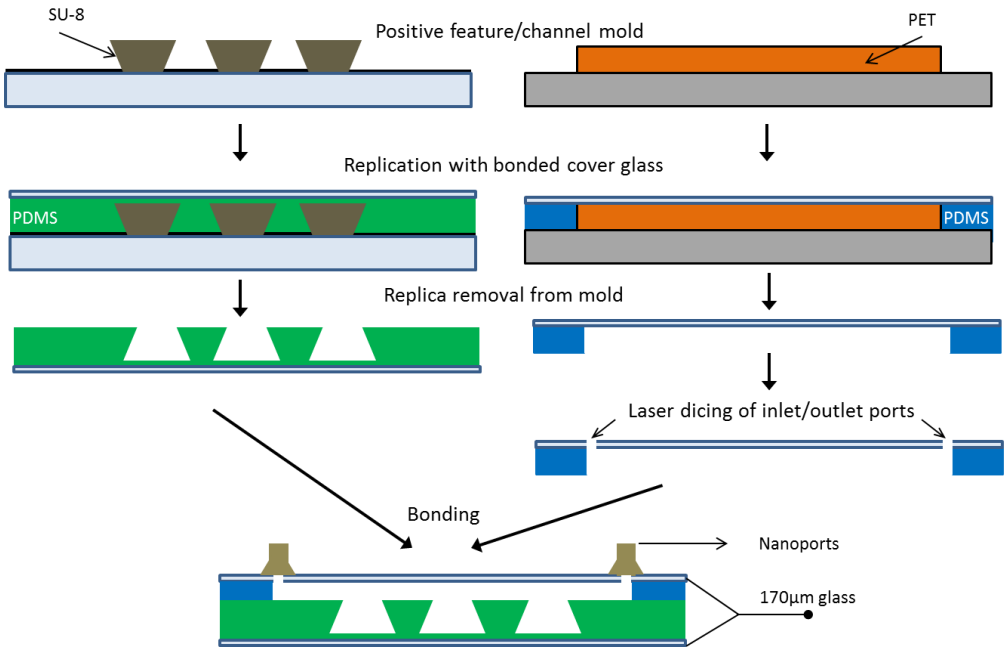

Figure 17: Stacked multilayer assembly process

3.6 Discussion

The fabrication of anisotropic trapezoidal microfeatures with various geometries was demonstrated using two methods: anisotropic etching of silicon and backside diffuser photolithography. The conditions for producing positive silicon mesa structures with minimal surface roughness and etching times were optimized by means of a three factor full factorial design of experiment. A method for creating an embedded chrome mask on a glass wafer was developed for the purpose of producing positive inverse-trapezoidal microfeatures out of a thick negative photoresist using backside diffuser photolithography. A simple and effective procedure for promoting the adhesion of the photoresist to the glass substrate was developed to increase the process yield. Lastly, the ability to control critical

dimensions and angles of the microfeatures produced by these two methods has been shown.

The two methods for microfeature fabrication were applied to develop two respective device assembly techniques. Each method utilized a different soft lithography technique. For each technique, protocols for facilitating mold detachment when using various replication polymers were developed, and the ability to integrate ultra-thin (<100 μm) replications with a 170 μm borosilicate glass backing—the fragile cover glass required for optical access—was demonstrated.

3.6.1 KOH etching design of experiment analysis

The data acquired from the full factorial experiment described in Chapter 3.1 was compiled and analyzed using the statistical analysis software, JMP (SAS Institute Corp). An analysis of variance (ANOVA) over the etch rate response variable was performed. The results indicated that the regression model of significant factors accounted for 93% of the total variability of etch rate. The F-statistic, which tested for the significance of the effects of the controlled factors and their interactions, was 31.94, indicating that these effects were significant with a p-value less than 0.001. The ANOVA for the second response variable, surface roughness, indicated that the regression model of significant factors accounted for 70% of the total variability of etch rate. The F-statistic was 5.169, which showed that the effects were statistically significant at a p-value less than 0.01. The

correlation between the controlled factors and the surface roughness response was not as representative as was the etch rate response. This can likely be attributed to the measurement error associated with measuring surface roughness values nearing the detection limit of the stylus profilometer. If higher resolution measurements were necessary, this experiment could be followed up utilizing instruments, like atomic force or scanning electron microscopes, capable of measuring nanoscale surface asperities.

The relationship between the factors indicated a strong correlation between etch rate and KOH concentration. As seen in the contour plot shown in **Figure 18**, the etch rate without sonication was 27.83 μm/hour at a KOH concentration of 35% by weight in 65 °C etchant solution. With sonication, however, the same concentration and temperature yielded an etch rate of 37.42 μm/hour. The combination of ultrasonic agitation, 30% KOH concentration, and 65 °C temperature was found to produce the fastest etch rate. **Figure 18** also shows that the surface roughness without sonication was elevated in the range of 20% to 35% KOH concentration at temperatures above 50 °C, peaking at 0.524 μm. With sonication, however, the surface roughness was significantly lower, with the lowest value being 0.0068 μm, obtained at a 40% KOH concentration and temperature of 65 °C. Therefore, the optimal conditions for low surface roughness are ultrasonic agitation, 40% KOH concentration, and an etching temperature of 65 °C.

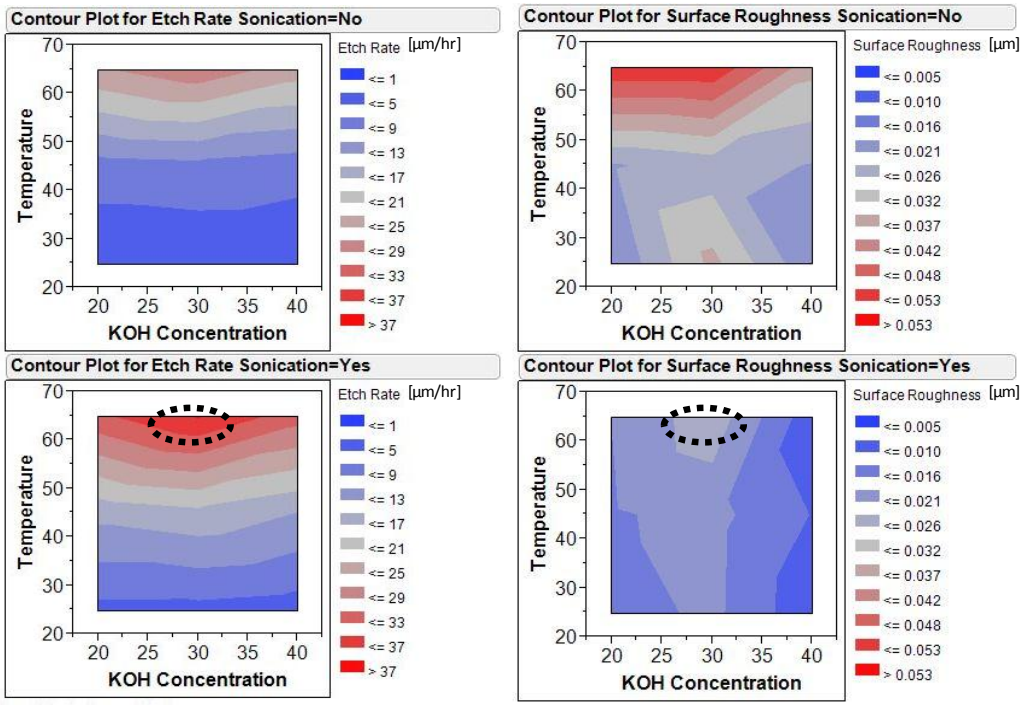

Figure 18: Contour plots for etch rate and surface roughness over the controlled factor space

Finally, a regression model was fit to the two response variables. The center points added to the design showed that there was a significant interaction between concentration and etchant temperature across the etch rate response variable, resulting in a model containing 2nd order approximations. The general form of the equation is given by **Equation 10**.

$$y = \beta_0 + \beta_1 x_1 + \beta_2 x_2 + \beta_3 x_3 + \beta_{23} x_{23} + \beta_{12} x_1^{\,2} + \beta_{13} x_2^{\,2} + \beta_{23} x_3^{\,3} \qquad \textbf{Equation 10}$$

where β_0 = y-intercept, β_i = coefficient term for i, β_{ij} = coefficient term for ij, x_1 = KOH Concentration, x_2 = Temperature, and x_3 = Sonication. Using the coefficient

estimates obtained from the JMP regression analysis, the resulting regression model equation:

$$y = 14.7 - 0.0490x_1 + 0.669x_2 - 3.03x_3 - 0.0783x_{23} - 1.35 \cdot 10^{-5} x_1^2 + 1.63 \cdot 10^{-5} x_2^2 + 2.58 \cdot 10^{-5} x_3^2$$ **Equation 11**

Conversely, the surface roughness response indicated no significant interactions between variables as no variable response curvature was seen. Therefore, the three main effects were the only factors included in the final regression model, and the coefficient estimates resulted in the model equation:

$$y = 0.0160 - 0.000327x_1 + 0.000346x_2 + 0.00742x_3$$ **Equation 12**

In summary, to optimize the anisotropic etching of silicon with potassium hydroxide, a full factorial design with two center points was conducted to test three factors: KOH concentration, temperature and agitation method. Optimal specifications for this process included a high etch rate, to reduce processing and fabrication times, and low surface roughness, to yield superior device functionality. The collected data show that the optimal etch rate conditions included 30% KOH concentration and 65 °C with ultrasonic agitation; and the minimum surface roughness conditions were above 40% KOH concentration and 65 °C with ultrasonic agitation.

3.6.2 Silicon sandwich assembly results

The cast polymer “sandwich” approach to fabrication, which included use of anisotropically etched silicon molds, offered several advantages including fast development time, simple fabrication technique, inexpensive material cost and minimal optimization. By developing an optimized silicon etching protocol, silicon trapezoidal structures with reproducible geometries were created and used for polymer replication as shown in **Figure 19**. The dimensional verification of the silicon trapezoidal geometry and the features replicated from it can also be seen in the figure. These images demonstrate that microfeatures with the undercut necessary to produce microvortical cell rotation can produce clean, replicated trapezoidal structures. These silicon structures can be bonded to a glass coverslip appropriate for imaging through the long back plane of the trapezoid.

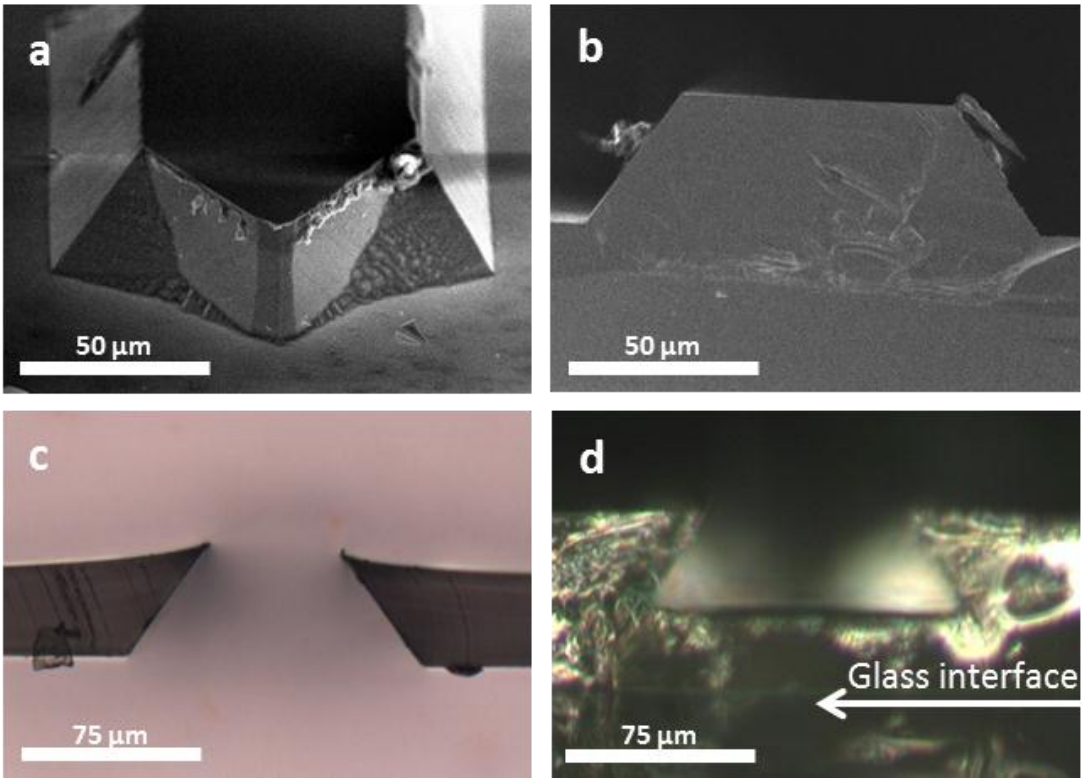

Figure 19 : Verification of the silicon microfeature geometry with subsequent replication and bonding. (a) Oblique view of silicon mesa; (b) Cross sectional view of silicon mesa; (c) Cross sectional view of a polymer replica; (d): Cross sectional view of a polymer replica bound to a glass substrate

However, the fragile nature of the silicon and borosilicate glass molds, combined with the delicate nature of ultra-thin polymer films, proved detrimental to device yield. When prying the two molds apart, the substrates frequently fractured or the polymer replicate tore. Substrate fracture was likely due to the high stress gradients introduced at the interface between the detached and attached portions of the wafer. In cases where the molds did not break, other failures experienced were thin-film tearing, unequal detachment and folding of the polymer-film back

on itself. The deficits of this protocol are attributable to the tenacity and fragility of ultra-thin polymeric replications over large surface areas. Because the total thickness of the replication polymer was only 100-150 microns, the effective surface area of the two, stacked molds dominated, and surface forces prohibited separation of substrates without tearing the polymer or breaking the substrate. Even after modifying the surface of the molds with anti-adhesion organosilanes that reduced the surface energy at the mold-polymer interface, the device yield was only 3% with a single device being fully assembled out of 29 assembly attempts.

In an attempt to overcome some of these challenges, a PDMS mold was created through a set of PDMS replication procedures to replace the silicon mold with a flexible replica. Briefly, an anti-adhesion silane (tridecafluoro-1,1,2,2-tetrahydrooctyl trichlorosilane; Gelest Inc.) was applied to the original silicon or glass mold to prevent PDMS adhesion. PDMS was poured over the mold and cured, and a PDMS negative several millimeters in thickness was obtained after thermal curing. The same silanization procedure was applied to the negative PDMS mold, resulting in a PDMS positive master with features identical to the original silicon mold. A PDMS mold offers the advantage of flexibility compared to a crystalline silicon mold, eliminating mold breakages. Because the mold is made of PDMS, there is no need to create the superficial PDMS monolayer required when using photocurable polymers for soft lithography. Lastly, because

PDMS has high oxygen permeability, an interesting effect is observed when the optical adhesive NOA 81 is used as the replication agent: After UV curing the polymer over the mold, a superficial layer of uncured polymer remains at the mold surface. As a result, the polymer can be directly bonded to a glass substrate after delaminating from the mold. It is hypothesized that because PDMS has high oxygen permeability, molecular oxygen inhibits the free radical polymerization in the UV adhesive, precluding crosslinking at the UV adhesive/PDMS interface (Bartolo, Degré, Nghe, & Studer, 2008). Unfortunately, the superficial layer of uncrosslinked material posed challenges. The trapezoidal features became rounded upon bonding the polymer replica to a glass substrate due to reflow of the uncrosslinked photopolymer at the glass-polymer interface. This reduction in feature sharpness is undesirable, especially when the corners at the trapezoidal feature inlet are compromised. The deformation of the inlet hinders the ability of the microfeature to peel off flow from the main channel and establish the recirculating flow profile necessary for cell rotation. In addition, the flexibility of the PDMS mold created challenges when compressing the two mold halves together. Often, the replication process produced a thin polymer membrane between the flow channel and the trapezoid inlet. This was likely the result of the fold over clips deforming the flexible mold, rather than properly distributing the compressive forces necessary to bring the surfaces of the two molds into uniform contact. In contrast, silicon and glass molds exhibit negligible deformation from the fold over clips, distributing compressive forces evenly across the mold.

3.6.3 Backside diffuser photolithography results

Backside diffuser photolithography (BDPL) offers distinct advantages over other anisotropic microfeature fabrication methods. Most importantly, the creation of positive undercut trapezoidal structures facilitates conventional molding techniques for producing an undercut negative polymer replica. The ability to directly produce a positive undercut microstructure with BDPL poses a distinct advantage over other trapezoidal fabrication techniques, such as the anisotropic etching of silicon, which require more complex replication procedures in order to produce the same geometry.

The BDPL technique normally utilizes negative photoresists with thicknesses no greater than 13 μm (J.-H. Lee et al., 2008) and has not been extended to thick (50 to 200 μm) negative resists. Because the ability to rotate microparticles larger than 10 μm requires a microchamber with a depth of at least 20 μm, thick negative photoresists were investigated. The most prominent negative photoresists for producing thick microfeatures are the SU-8 2000 series or the KMPR-1000 series which have the ability to produce resist thicknesses of up to 200 μm (Microchem Corp.). However there are no prior reports of using either photoresist line in frontside or backside diffuser lithography.

Initially, KMPR 1025 was investigated because reports demonstrated its superior adhesion to glass substrates compared to SU-8 (Hou, Zhang, Smith, Yang, & Heikenfeld, 2010). The adhesion of the photoresist to the substrate is critical when

using thick photoresists because the thermal cycling in the post-exposure bake introduces large stresses at the material interface as a result of the shrinking of the resist during cross-linking. When using KMPR for BDPL, slight variations in the fabrication process described in Chapter 3.3 were required. Therefore a protocol for producing 40 μm KMPR microfeatures was adopted from Ray *et al* (Ray, Zhu, & Meldrum, 2010). The only variation in the process flow was the use of larger exposure doses, ranging from 2000 to 4500 mJ/cm^2 to compensate for optical losses introduced by the diffuser. In addition, when using BDPL, large exposure doses are essential if it is desired to produce linearized sidewalls in the exposed portion of the resist because the maximum diffusing angle of the UV light through transparent portions of the embedded mask and the photoresist thickness are fixed. Underexposure can result in oblique 3D features that lack a sharp edge at the back edge of the trapezoid in addition to rounded sidewalls (J.-H. Lee et al., 2008).

Although the KMPR resist exhibited excellent adhesion to the glass substrate, the 3D microstructure formed was not the expected inverse-trapezoidal cross section.

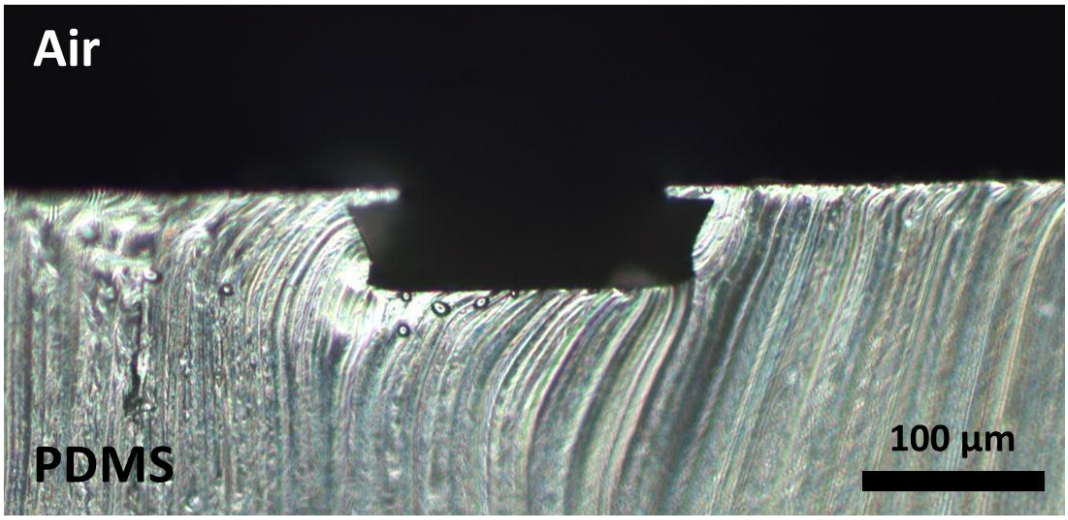

Figure 20: Cross sectional geometry of KMPR following backside diffuser photolithography and replicate molding

The cross sectional feature geometry was documented by means of replication and cutting down the middle of the polymer microfeature with a sharp blade. The result is shown in **Figure 20**. To ensure the photoresist had not being underexposed, exposure doses over three times that reported in the literature were used, yet microfeatures nearly identical in form to the one illustrated in **Figure 20** were produced. Other modifications to the baking protocols failed to affect the geometry. Six wafers produced the same or similar cross sectional geometry despite only slight variations to the published protocol. Given that BDPL had never been applied to this photoresist and that the other publications applying BDPL never reported any similar complications, the use of the KMPR resist was abandoned, the results obtained remaining unexplainable.

Another thick negative photoresist, SU-8 2035 was then investigated for use in the BDPL process. As indicated earlier, poor adhesion between SU-8 and glass substrates had been identified by other researchers as problematic. Initial attempts to produce SU-8 trapezoidal microfeatures resulted in complete delamination of the resist from the glass substrate during development. To eliminate this common failure, an adhesion promotion protocol to increase the bond strength between the photoresist and the substrate was investigated. The most common solution prescribed a lengthy process to create a thin SU-8 that blanketed the entire wafer (J Carlier et al., 2004). Further modifications of this protocol incorporated additional surface modification steps (Julien Carlier et al., 2006). While these methods had been shown to increase the bond strength of the SU-8, a much simpler, less time consuming method was pursued.

Since SU-8 (bisphenol A diglycidyl ether) is an epoxy resin containing reactive epoxide groups, conjugation between a functionalized glass surface and the resist was realized by a simple surface modification technique that utilized common laboratory reagents and was completed in less than 30 minutes. Epoxy resins that are catalytically crosslinked, rather than photoinitiated as in the case of SU-8, utilize primary or secondary amines as curing agents. Also, a coupling agent commonly found in research and laboratory settings is an amine terminated silane (APTES). Interestingly, there were no previous reports of using APTES to directly promote the adhesion of SU-8 to glass wafers for photolithography. Yet several reports had demonstrated the use of APTES to facilitate bonding PDMS

and other plastics to SU-8 (Vlachopoulou et al., 2009; Z. Zhang, Zhao, Xiao, Watts, & Xu, 2011) or for coupling silica beads to epoxy resins (Meador et al., 2005). Conceptually, the requirements for conjugating PDMS or silica beads to epoxy resins are identical to those for coupling SU-8 to a glass substrate. Therefore, a simple method for rapidly modifying the surface of the glass wafers with APTES to promote the adhesion of the SU-8 was developed and utilized in the BDPL process. By incorporating this step, the SU-8 microfeatures did not detach when developing the resist, and were permanently bound to the glass substrate after hard baking.

A unique feature of BDPL is the ability to modulate the sidewall angle (the angle formed by the side of the trapezoid with respect to the main flow channel) of the trapezoidal features by simply changing the index matching liquid (IML) used to couple the diffuser to the back of the chrome-patterned wafer. The ability to easily produce a desired sidewall angle may be unique to this method and is not feasible when using silicon etching methods. The sidewall angle is dictated by Snell's Law, where the IML determines the angle of refraction and subsequently the maximum diffusing angle of the UV light as it enters the photoresist. As described in Chapter 2, the sidewall angle significantly influences the characteristics of a microvortex. The ability of BDPL to precisely control the angles of the trapezoids is a distinct advantage for producing optimal microvortical properties. The ability to specify the trapezoid is shown in **Figure 21**. When DI water (n=1.33) was used

as the IML, a trapezoidal feature with a sidewall angle of 56° was produced. When using mineral oil (n=1.47) as the IML, a trapezoid angle of 46° resulted.

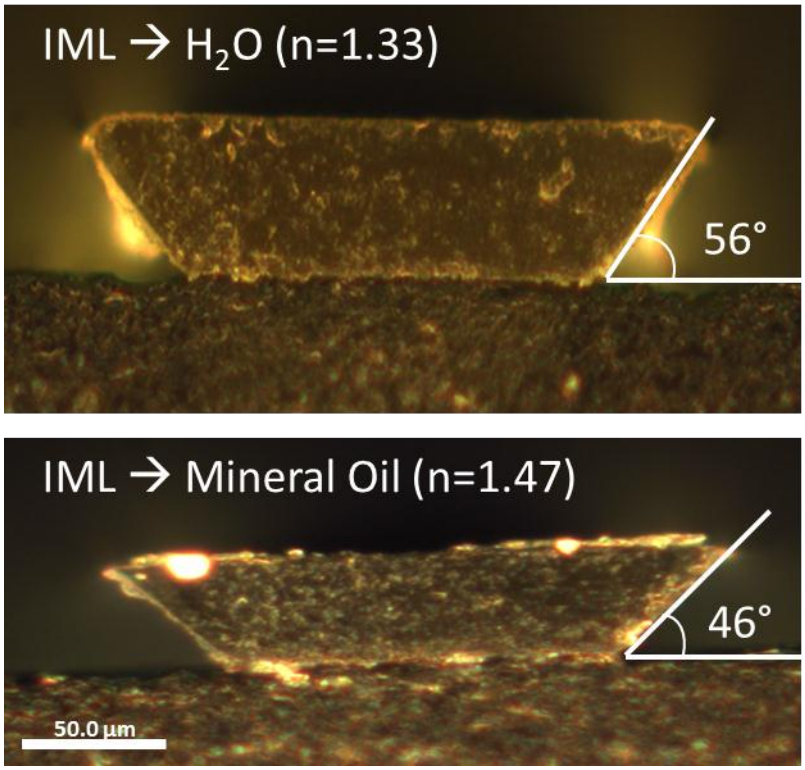

Figure 21: Changing the index matching liquid (IML) to create variable sidewall angles

3.6.4 Stacked multilayer assembly results

The stacked multi-layer assembly method avoided many of the issues encountered in the "silicon sandwich" assembly approach. Because replication of the channel mold and the mold containing the microfeatures are independent processes, any problems encountered with one did not affect the other (shown in **Figure 22**). The replication of the trapezoidal microfeatures in PDMS was successful in producing

microfeatures with inlet widths ranging from 40 -120 µm and heights of 40 – 80 µm. The backside face of the trapezoid was smooth and parallel to the channel, making it amendable to imaging through the surface.

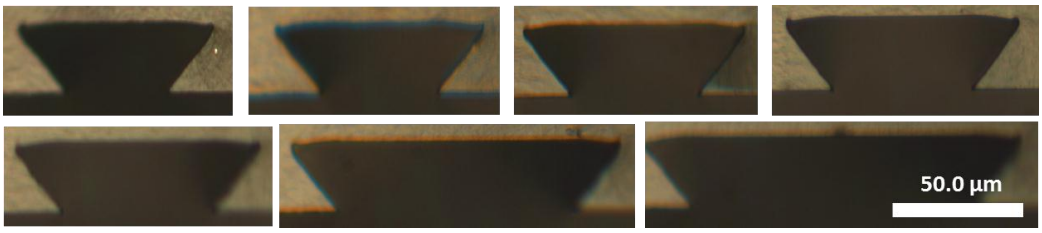

Figure 22: PDMS replications of inverse trapezoid features with varying inlet widths

However as seen in **Figure 23** , the ability to fully displace the PDMS between the backside of the trapezoid and the surface of the cover glass was problematic, and often a 10 to 50 µm layer remained despite applying a weighted load to compress them**.** However in the case of the flow channel, no residual PDMS film could be seen after replication. This could be due to several factors such as the difference in the mold material, the difference in aspect ratio of the features, or the difference in the effective surface area.

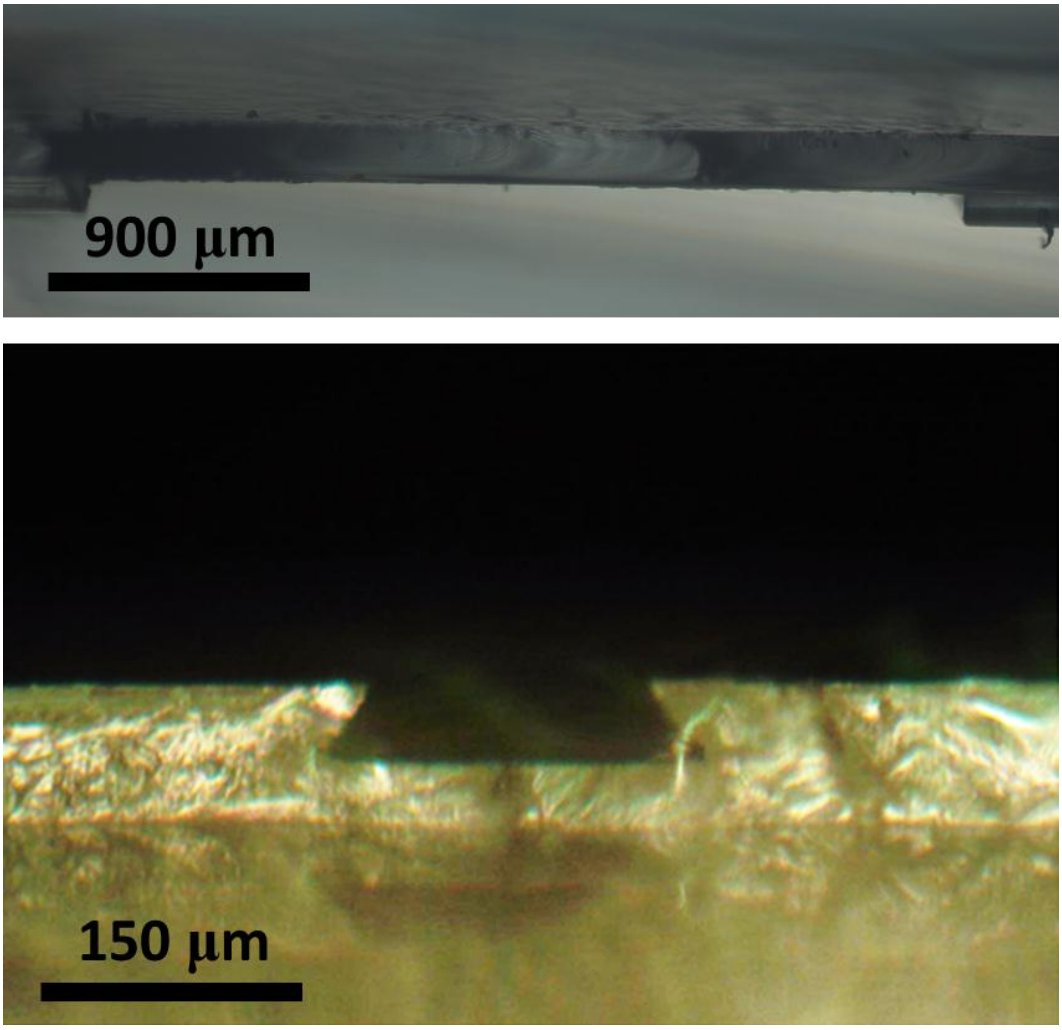

Figure 23: Cross sectional images of replicated (top) flow channel and (bottom) trapezoidal microfeatures

The channel replication yield was around 80%, after improvement, due to the use of the flexible, laser fabricated mold. The 20% failures, which usually occurred after demolding, were the result of trimming PDMS displaced from beneath the cover glass or when cleaning the surface before bonding. However, the microfeature replication yield was substantially lower, at around 25% when

forming the ultra-thin negatives on a cover glass substrate. The inflexibility of the glass substrate combined with the fragile cover glass made it difficult to detach the mold without chipping or cracking occurring in the cover glass. One solution is to produce a PDMS positive mold through the multiple-replication process described at the end of Chapter 3.6.2.

The successful assembly of the device can be seen in **Figure 24**.

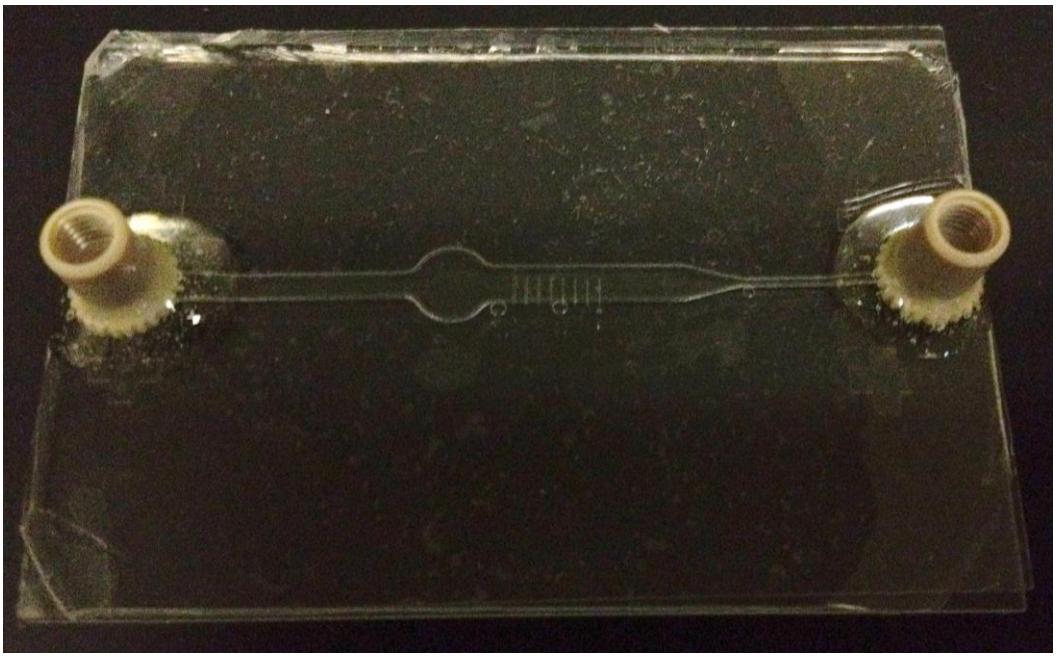

Figure 24: Fully assembled device using the stacked multi-layer technique

Chapter 4: Systems Integration

4.1 Custom pump design and development

Microfluidic systems can perform a variety of fluid manipulations. Fundamental to their function is the ability to accurately control the transport of fluid from one location to another. Microscale transport has been demonstrated by a variety of mechanisms; however most pumping methods have been categorized into one of two main classifications: mechanical displacement or electro- and magneto-kinetic (Iverson & Garimella, 2008). While some electro- and magneto-kinetic pumping options offered attractive features such as bi-directional flow capability, and non-pulsatile flow at low flow rates (sub nL/min), the underlying complexity in the working mechanism was limiting. For instance, electroosmotic flow regulators require a special surface treatment in the microchannel to work properly. In addition, electrokinetic devices require the use of special driving media, with various conductivities and pH values. When considering traditional mechanical displacement pumps, which included using diaphragms, rotary gears, and stepper motors, the flow stability was poor and often pulsatile.

The stability and consistency of the recirculating flow in the microvortex is directly dependent on the flow characteristics delivered by the pump. Exquisite control over the flow velocity in the main flow channel is imperative to produce stable and precise cell rotation by means of a fluidic vortex. A pressure driven pumping system provides the bi-directional, pulse-free characteristics offered by

electro- and magneto- kinetic pumps while avoiding the limitations associated with utilizing specific buffers or surface chemistries. We designed a pump that uses both positive and negative pressure regulators to produce flow of a driving fluid that is metered and then used to drive solutions of cell-containing media through the microfluidic device as seen in **Figure 25.**

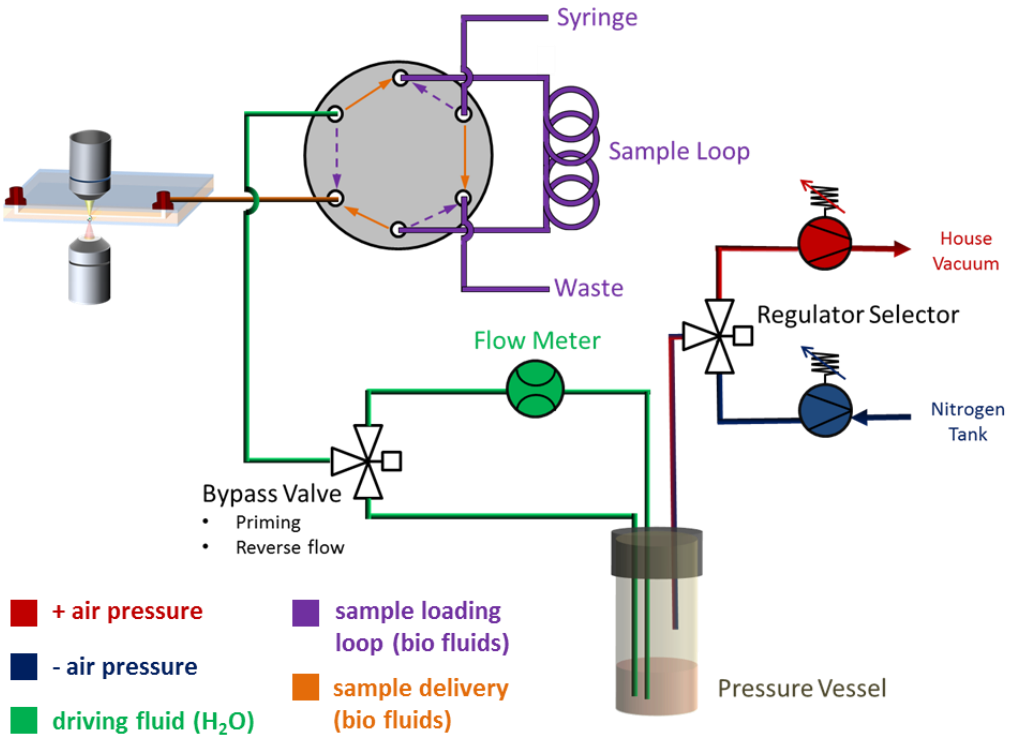

Figure 25: Pressure-driven pump schematic

The pressure regulators (QPV-1, Proportion-Air Inc.) were electro-pneumatic precision pressure proportional control valves and were used to pressurize a custom built 50 mL test tube (pressure vessel). A three way valve (LHDA002000B, The Lee Company) was used to select between the positive and

the negative pressure lines. An in-line flow meter (SLG1430-025, Sensirion Inc.) with sub nanoliter resolution was used to measure the liquid flow rates produced. Another three-way valve was used to bypass the flow sensor when necessary, due to the large pressure drop across it. Finally, a 6-port, 2-way valve (MXP7900-000, IDEX Inc.) was used as a sample injection valve. This valve functions to introduce biological media only immediately upstream of the microvortex chip, avoiding any complications with the flow sensor, which required the use of water only as a driving fluid.

The pressures required to produce flow rates spanning the detection range of the flow sensor (50-1500 nL/min) were determined prior to purchasing the pressure regulator to ensure the controlled pressures were adequate. This was accomplished by building the simple pressure monitoring circuit shown in **Figure 26**. The pressure range to be controlled by the pressure regulator was determined by recording the local pressure at a location upstream from the pressure vessel, effectively replacing the positive pressure regulator seen in **Figure 25**, and the flow rate from the flow meter. The pressure vs. flow rate relationship was also found to be highly linear as shown in **Figure 27.** A pressure of around 23 psi was needed to reach the sensor's maximum flow rate detection limit.

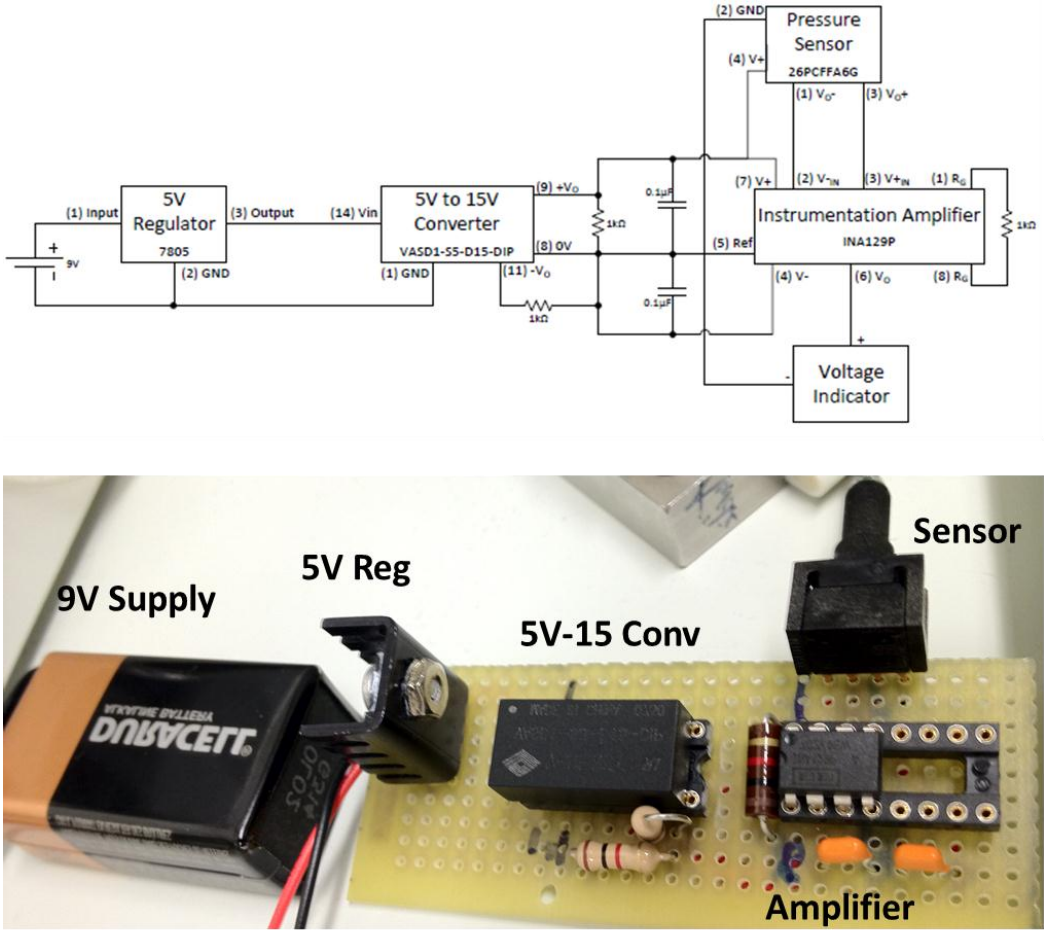

Figure 26: Pressure sensing circuit for pump regulator selection

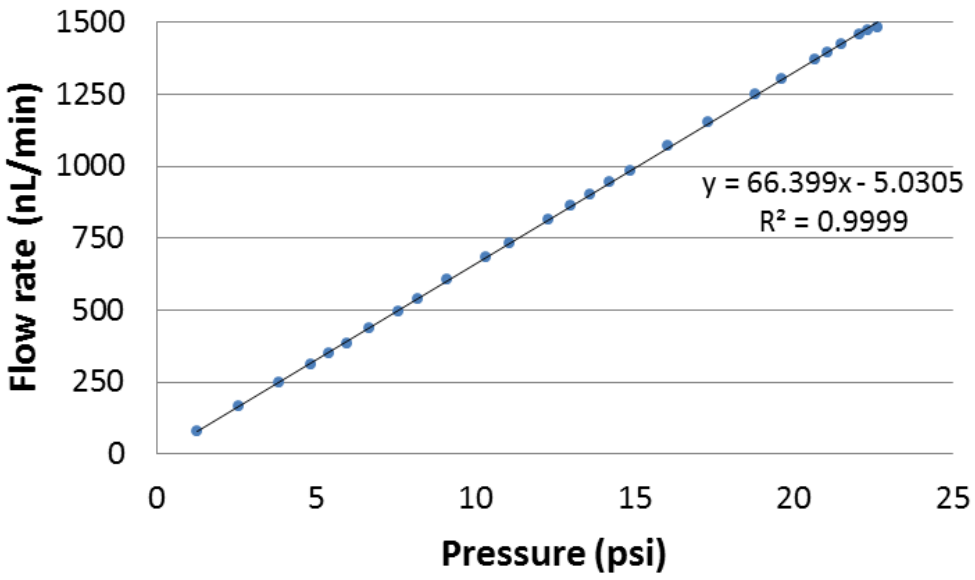

Figure 27: Flow rate vs. pressure as determined by the pressure sensing circuit

4.1.1 Custom pump characterization and results

Pump metrics were determined by a set of two experiments. Software developed (Dean Smith, Center for Biosignatures Discovery Automation) in Labview 2010 (National Instruments Inc.) was used to record the flow rate from the meter, control the valve positions, and control the pressure-regulating voltages, while saving the information into a spreadsheet allowing accurate measurements of component input and output values versus time. The first experiment was used to determine the response time of the pump to changes in pressure. Time constants associated with switching from zero flow to maximum positive flow, maximum flow to zero flow, zero flow to maximum negative flow, and maximum negative

flow to zero flow were quantified. An example graph of flow rate vs. time in response to step changes in driving pressure is shown in **Figure 28**. This same trace was replicated three additional times to determine the average response time of 363 ± 34 ms.

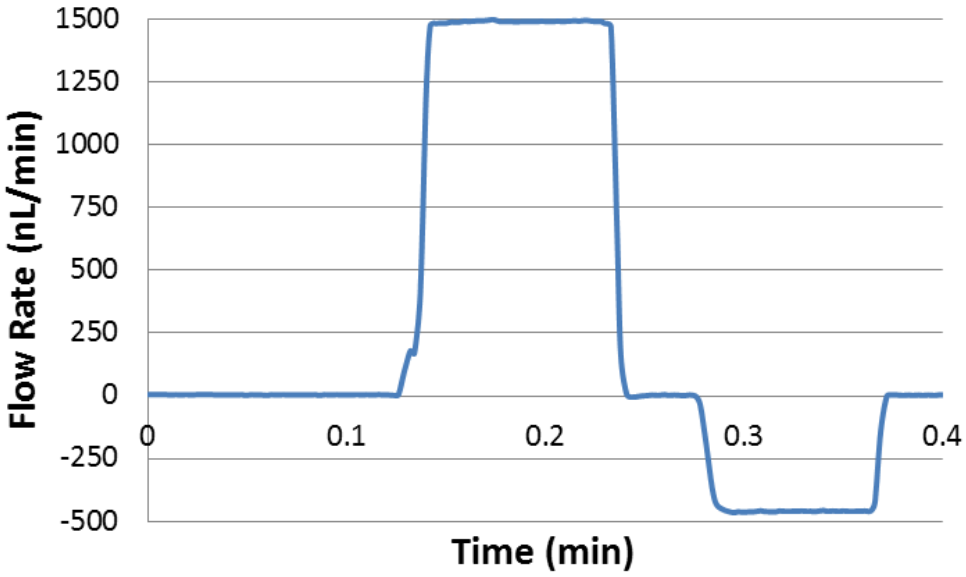

Figure 28: Flow rate vs. time in response to step changes in pressure

The second experiment was designed to determine the average variability in the flow rate over time. Three different pressures were set, resulting in three different flow rates that were measured over 2 minutes as seen in **Figure 29**. The standard deviation and the mean flow rate were determined, and the average variability (time average deviation from the mean) was found to be 2.6% over the period of 2 minutes.

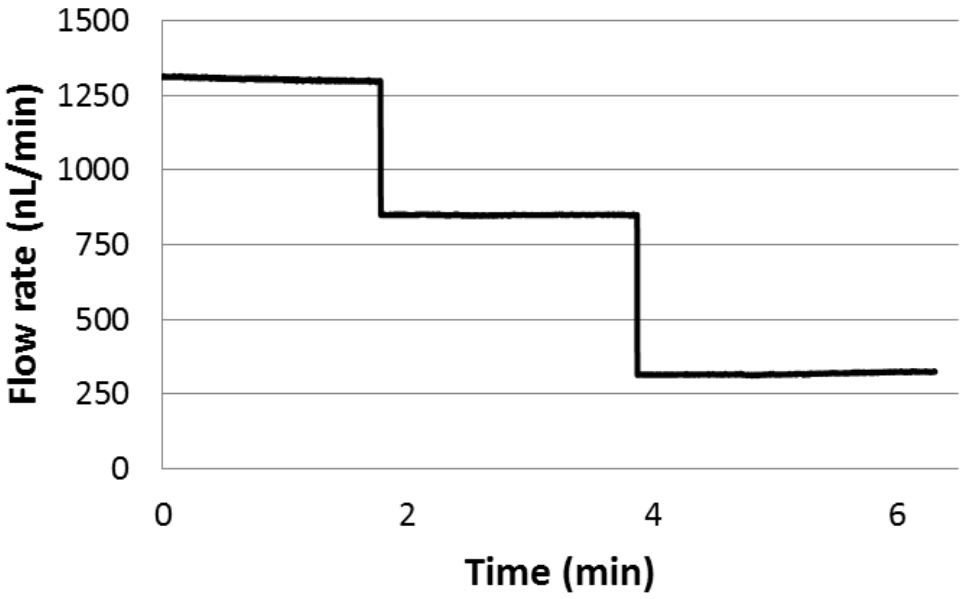

Figure 29: Flow rate variability measurement at three different flow rates

4.2 Infrared optical trapping and imaging configuration

Manipulation of the microparticles into the microvortex center was accomplished by an optical tweezing setup. The optical trapping system and the imaging components are shown in **Figure 30.** A 1064 nm diode laser (LDF-1064-BF-600, Innolume GmbH) was coupled to a beam expander to produce a 12 mm collimated beam, which was reflected off a 825 nm short pass dichroic mirror (Omega Optical Inc.) into a 40X, high numerical aperture objective lens (MRD77410, Nikon Instruments Inc.) that focused the beam onto the specimen from above. A Xenon lamp white light source was coupled to an inverted Nikon TI-S microscope and focused through a 40X air objective lens (not shown). The

light transmitted through the specimen was collected by a CMOS camera (DCC1545C, Thorlabs).

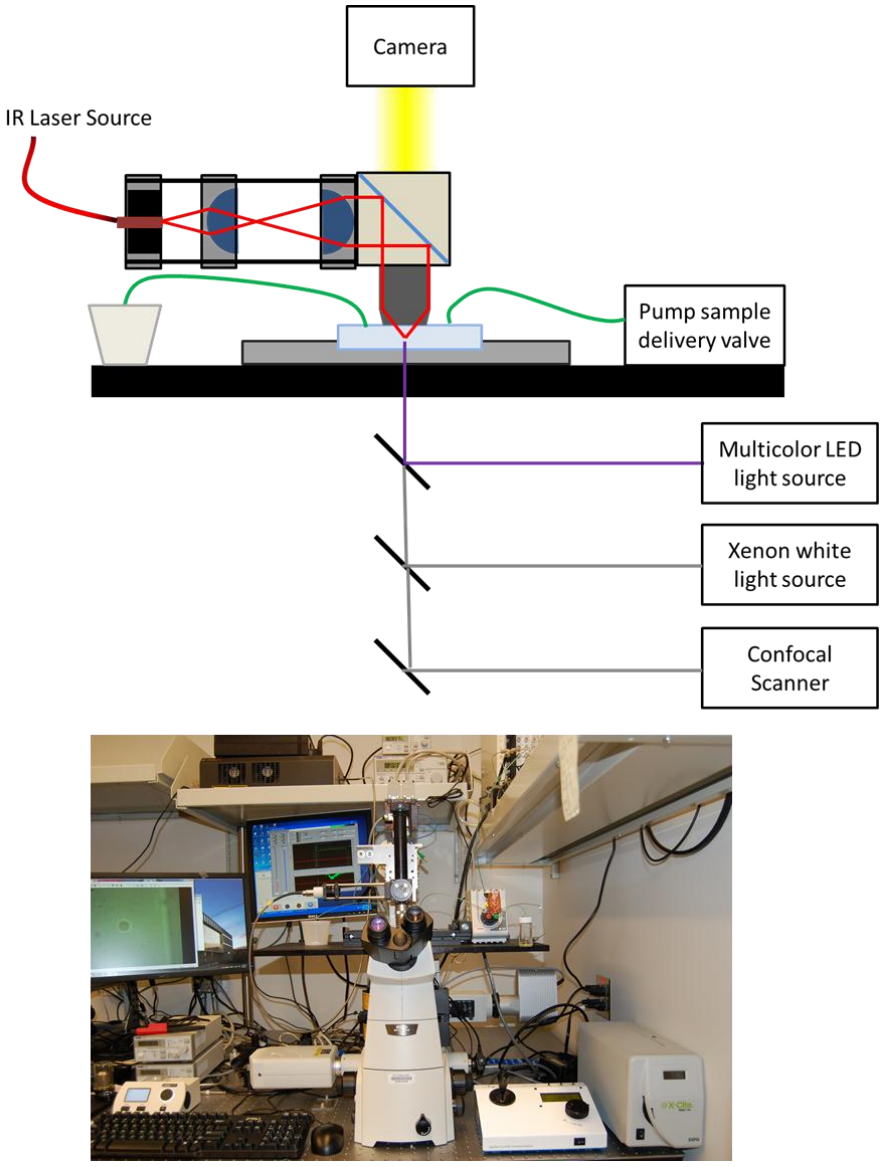

Figure 30: Optical configuration for tweezing and imaging (top) light path schematic (bottom) experimental setup

4.2.1 Imaging and trapping considerations for cell rotation

Focused beams of the top optical trapping objective and the bottom imaging objective were susceptible to interference given the inherent geometries of the trapezoid microvortex. A summary of potential interference configurations is shown in **Figure 31**. This was considered during the design of the microvortex chip, as losses in the high angle rays of the optical trap result in a decrease in intensity gradient along the axis of the beam, compromising the z-force of the optical trap. Additionally, clipping of the high angle imaging beam results in a significant reduction in resolution, and could result in aberrations when acquiring projections.

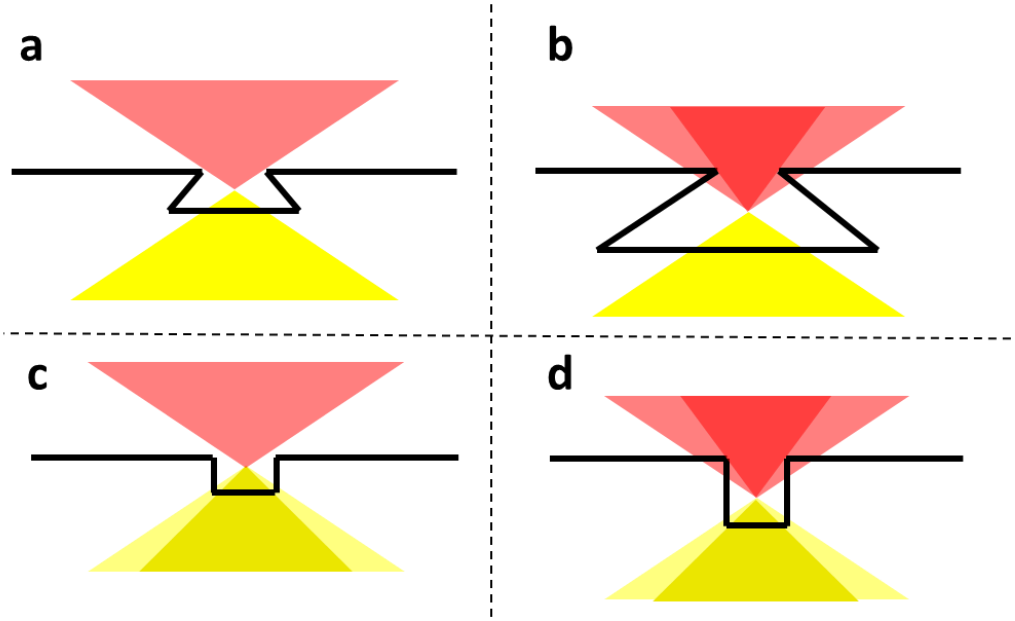

Figure 31: Optical obstruction of the optical tweezers or the imaging light based on microchamber geometry (a) no obstruction (b) top obstruction (c) bottom obstruction (d) both top and bottom obstruction

4.3 Proof of concept demonstration

As shown in **Figure 32**, the combined product of the microfabrication methodologies, the infrared optical trap, and the imaging capabilities provided the first demonstration of microparticle rotation by a microvortex about an axis parallel to the imaging plane. While it was difficult to perceive the rotation when viewing the smooth spherical surface of a 15 μm bead, this demonstration had a small artifact aligned with the rotation axis that made the rotation more visible. Similarly, a single K562 (immortalized human myelogenous leukemia) cell was rotated in the 3D microvortex as shown in **Figure 33**.

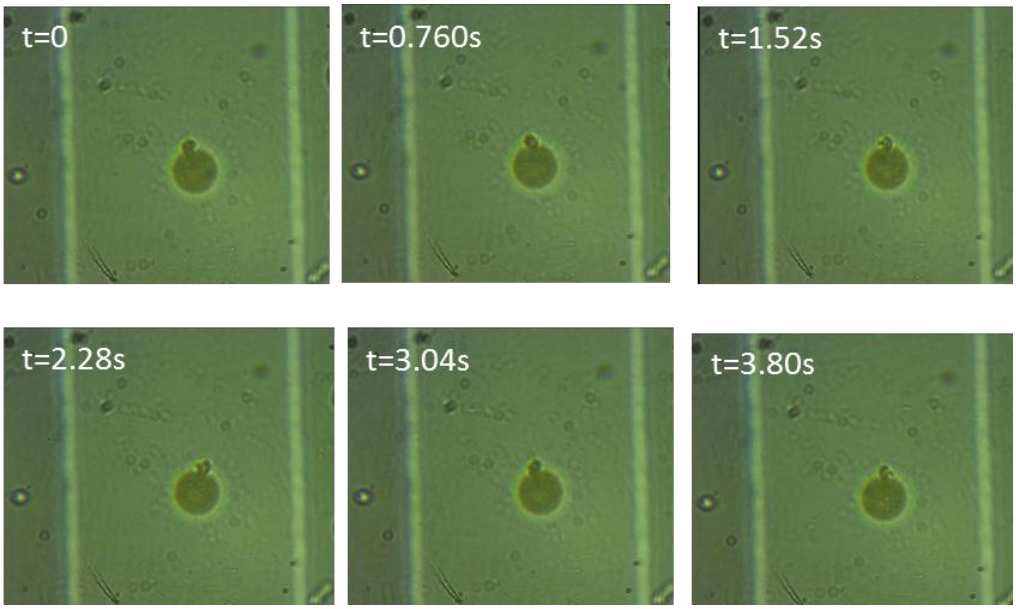

Figure 32: Demonstration of a 15 µm bead being rotated in a 3D microvortex

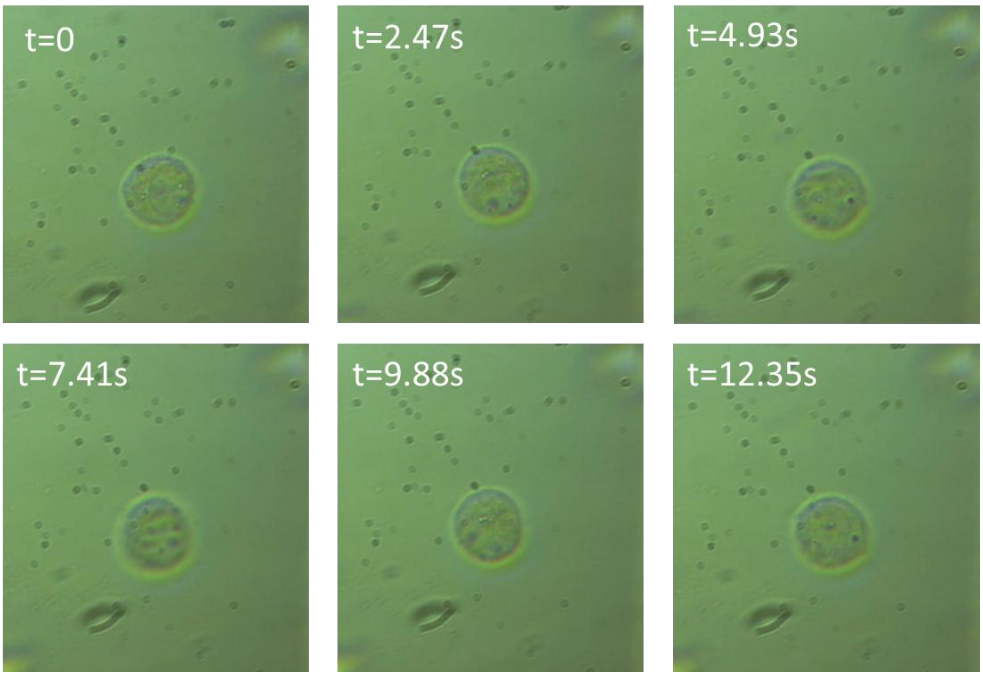

Figure 33: Demonstration of a leukemia cell being rotated in a 3D microvortex

Chapter 5: Conclusion and future work

5.1 Summary of work completed

The work reported in this thesis has demonstrated the ability to use hydrodynamic microvortices for controlled rotation of microparticles about an axis parallel to the imaging plane. The microchamber geometries capable of producing stable recirculating flow profiles were determined experimentally, using a 2D side-channel microvortex chip, and theoretically, with the aid of computational fluid dynamics (CFD) using COMSOL Multiphysics software. The CFD models gave insight regarding the effects of the sidewall angle and the aspect ratio of the microchamber on the location of the microvortex center, the rotation rate of a particle at the center, and the maximum shear rate on the particle surface.

Two fabrication and assembly techniques were developed to produce a 3D microvortex chamber and chip. The first utilized anisotropic etching of silicon to produce positive mesa structures which were then compressed against a positive glass channel counterpart to form a mold. The mold was then replicated to create a polymer negative, and the device was sealed by bonding 170 μm microscope coverglass to both sides. This approach was replaced by the second method, which applied backside diffuser photolithography (BDPL) to produce undercut inverse trapezoids in photoresist on a glass surface to serve as the mold. The process was optimized for SU-8 2035, a thick negative photoresist, and required the development of an adhesion promotion protocol to ensure the microstructures

remained intact during processing. The positive SU-8 mold was then used to create ultra-thin (<100μm) trapezoid replications with a coverglass backing, and a main flow channel with a coverglass backing was formed in a similar fashion by replicating a laser cut PET mold. Finally, the two replicated halves were bonded together to form the 3D microvortex chip.

Lastly, a novel air pressure-regulated pump was designed and characterized. The pump allowed for bidirectional flow manipulation at flow rates ranging from 100-1500 nL/min. The time average variation in the flow was 2.6% over two minutes, and the average step response time was 363 ms. The ability to produce constant low particle velocities, and the ability to bring the particle to zero velocity in less than a second was demonstrated.

5.2 Future characterization of cell rotation

The most important work that has yet to be completed is the characterization of cell rotation rate versus the flow rate in the main channel. As an extension, this relationship should be characterized for microfeatures with various sidewall angles and aspect ratios. How cell size and shape impact the rotation rate should also be investigated. Furthermore, the incident power of the optical trap should be reduced to a minimum, to deliver just enough power to hold the cell at the vortex center so that it is not swept away. The minimum level will likely vary at different flow rates and in different geometries, requiring characterization.

5.3 Measurement of local heating in an optical trap

Laser induced heating in optical traps has been modeled and measured in several different instances (Peterman, Gittes, & Schmidt, 2003), and others have proposed methods to control the effects of the heating through active cooling elements (Mao, Arias-Gonzalez, Smith, Tinoco, & Bustamante, 2005). In general, the reported temperature increase due to heating by the trapping beam ranged from 1-4°C/100mW of incident laser power. However, these reports do not consider the convective heat transfer from the recirculating fluid flow in a microvortex, so the degree of temperature increase is not certain. Two methods for measuring the local heating have been proposed. The first uses temperature sensitive fluorescent probes dissolved in the media to measure the temperature distribution within the optical trap (Ross, Gaitan, & Locascio, 2001). The other exploits phase transition temperatures to quantify the temperature change. Briefly, microemulsions of materials (paraffin or similar) containing various melting points ranging from 25-45°C are produced by heating the material past its melting point in an insoluble liquid (water) and shaking the solution vigorously. The material is then "flash" solidified by rapidly pouring in chilled (4°C) water. The result is 2 to 20 μm solid emulsions of paraffin in water. The emulsions are then filtered out, dried, and characterized by measurement with a differential scanning calorimeter. This can determine the required energy per mass to melt the material at a given temperature. Finally, the microemulsions are irradiated with the optical trap at different incident powers until a visible change from the crystalline texture

of the solid material to the clear smooth texture of the melted material can be seen. This method offers the possibility of incorporation into the use of a microvortex to better simulate the heat dissipation that results from the convective fluid flow.

5.4 Future microfabrication development

Backside diffuser photolithography (BDPL) is a new field with significant opportunity for innovation. One unique property of the technique is its ability to modulate sidewall angle, as demonstrated by this thesis; another feature that was not exploited is its ability to create rounded sidewalls, or features with elliptical cross-sections. In theory, rounded trapezoid corners can be produced by applying a lower exposure dose. This is due to the integration effect of the exposure of the photoresist, where the middle of the feature is being maximally exposed over time, while the maximally diffused rays into the photoresist receive the minimum dose per unit time. The diffusing angle and the thickness are fixed, and the exposure dose dictates the total cross-linking profile(J.-H. Lee et al., 2008). This could allow trapezoids to be fabricated with rounded corners, while still possessing the flat back surfaces necessary for cell imaging. These microchambers may provide superior vortex stability due to the increase in circularity of the recirculating flow.

5.5 Future integration of optical fiber tweezers

The current microvortex design utilized a single-beam gradient-force optical trap. However, another possible optical trapping mechanism would utilize counter-propagating dual beams delivered through opposing aligned optical fibers. The trap is created in a region where the beams are diverging, reducing the light intensity relative to a focused beam. This, in turn, reduces the likelihood of optical damage. Counter propagating optical fibers decouple the trapping mechanism from the microscope, reducing both cost and footprint of the platform. The optical arrangement for the dual optical fiber trapping setup is described as follows. In brief, a linearly polarized 1064 nm light source is passed through a ½ wave-plate to resolve two waves perpendicular to each other. The waves are then split by a polarizing splitter and coupled into two optical fibers. The fibers are then counter aligned and their separation controlled by a single axis micromanipulator. The distance between the fibers must be optimized for particles of different sizes due to the divergent profile of the beam exiting the fiber. The fibers could be self-aligned by the angled edge of the trapezoid and can be fed through the trapezoidal feature into the microfluidic. This opens up the possibility of creating multiple channels with multiple optical fibers, allowing several cells to be rotated simultaneously in parallel channels. The imaging objective would scan between the channels to image when necessary.

5.6 Conclusion

This thesis has demonstrated the groundwork for a live cell rotation imaging chamber taking the form of a microscope stage-mounted chip. Contributions in microfluidic fabrication, in conjunction with the development of a precision pump, have provided a chip-based-system for cell introduction and delivery through a main flow channel, having below it, disposed towards a high-magnification objective lens of the cell imaging system, an optically-addressable trapezoidal microchamber. Individual cells can be maneuvered from the main flow channel, through the inlet neck, into the trapezoidal chamber, in which a microvortex is formed by the peeling off of flow streamlines from the bottom surface of the main flow channel. Multiperspective absorption or fluorescence imaging can be procured through low, rotational, tangential, fluidic shear forces induced on the cell, while stabilized in an optical trap.

REFERENCES

Avery, S. V. (2006). Microbial cell individuality and the underlying sources of heterogeneity. *Nature reviews. Microbiology*, *4*(8), 577-87. doi:10.1038/nrmicro1460

Baek, S., & Song, S. (2011). A one-step photolithography method for fabrication of a staggered herringbone mixer using inclined UV lithography. *Journal of Micromechanics and Microengineering*, *21*(7), 077001. doi:10.1088/0960-1317/21/7/077001

Bartolo, D., Degré, G., Nghe, P., & Studer, V. (2008). Microfluidic stickers. *Lab on a chip*, *8*(2), 274-9. doi:10.1039/b712368j

Carlier, J, Arscott, S., Thomy, V., Fourrier, J. C., Caron, F., Camart, J. C., Druon, C., et al. (2004). Integrated microfluidics based on multi-layered SU-8 for mass spectrometry analysis. *Journal of Micromechanics and Microengineering*, *14*(4), 619-624. doi:10.1088/0960-1317/14/4/024

Carlier, Julien, Chuda, K., Arscott, S., Thomy, V., Verbeke, B., Coqueret, X., Camart, J. C., et al. (2006). High pressure-resistant SU-8 microchannels for monolithic porous structure integration. *Journal of Micromechanics and Microengineering*, *16*(10), 2211-2219. doi:10.1088/0960-1317/16/10/039

Chapman, J.-A. W., Miller, N. a, Lickley, H. L. a, Qian, J., Christens-Barry, W. a, Fu, Y., Yuan, Y., et al. (2007). Ductal carcinoma in situ of the breast (DCIS) with heterogeneity of nuclear grade: prognostic effects of quantitative nuclear assessment. *BMC cancer*, *7*, 174. doi:10.1186/1471-2407-7-174

Cohen, a a, Geva-Zatorsky, N., Eden, E., Frenkel-Morgenstern, M., Issaeva, I., Sigal, a, Milo, R., et al. (2008). Dynamic proteomics of individual cancer cells in response to a drug. *Science (New York, N.Y.)*, *322*(5907), 1511-6. doi:10.1126/science.1160165

Conchello, J.-angel, & Lichtman, J. W. (2005). Optical sectioning microscopy, *2*(12). doi:10.1038/NMETH815

Cummings, E. B., & Singh, A. K. (2003). Dielectrophoresis in microchips containing arrays of insulating posts: theoretical and experimental results. *Analytical chemistry*, *75*(18), 4724-31. Retrieved from http://www.ncbi.nlm.nih.gov/pubmed/14674447

Dalerba, P., Dylla, S. J., Park, I.-K., Liu, R., Wang, X., Cho, R. W., Hoey, T., et al. (2007). Phenotypic characterization of human colorectal cancer stem cells. *Proceedings of the National Academy of Sciences of the United States of America*, *104*(24), 10158-63. doi:10.1073/pnas.0703478104

Darzynkiewicz, Z., Bedner, E., Li, X., Gorczyca, W., & Melamed, M. R. (1999). MINIREVIEW Laser-Scanning Cytometry : A New Instrumentation with Many Applications, *12*, 1-12.

Evander, M., Johansson, L., Lilliehorn, T., Piskur, J., Lindvall, M., Johansson, S., Almqvist, M., et al. (2007). Noninvasive acoustic cell trapping in a microfluidic perfusion system for online bioassays. *Analytical chemistry*, *79*(7), 2984-91. doi:10.1021/ac061576v

Fauver, M., Seibel, E., Rahn, J. R., Meyer, M., Patten, F., Neumann, T., & Nelson, A. (2005). Three-dimensional imaging of single isolated cell nuclei using optical projection tomography. *Optics express*, *13*(11), 4210-23. Retrieved from http://www.ncbi.nlm.nih.gov/pubmed/19495335

Gosse, C., & Croquette, V. (2002). Magnetic tweezers: micromanipulation and force measurement at the molecular level. *Biophysical journal*, *82*(6), 3314-29. Elsevier. doi:10.1016/S0006-3495(02)75672-5

Helmchen, F., & Denk, W. (2005). Deep tissue two-photon microscopy. *Nature methods*, *2*(12), 932–940. Nature Publishing Group. doi:10.1038/NMETH818

Hou, L., Zhang, J., Smith, N., Yang, J., & Heikenfeld, J. (2010). A full description of a scalable microfabrication process for arrayed electrowetting microprisms. *Journal of Micromechanics and Microengineering*, *20*(1), 015044. doi:10.1088/0960-1317/20/1/015044

Iverson, B. D., & Garimella, S. V. (2008). Recent advances in microscale pumping technologies: a review and evaluation. *Microfluidics and Nanofluidics*, *5*(2), 145-174. doi:10.1007/s10404-008-0266-8

Kim, J., Seidler, P., Wan, L. S., & Fill, C. (2009). Formation, structure, and reactivity of amino-terminated organic films on silicon substrates. *Journal of colloid and interface science*, *329*(1), 114-9. Elsevier Inc. doi:10.1016/j.jcis.2008.09.031

Kreysing, M. K., Kießling, T., Fritsch, A., Guck, J. R., Josef, A. K., Zeiss, C., & Gmbh, M. (2008). The optical cell rotator Abstract :, *16*(21), 912-914.

Le Saux, B., Chalmond, B., Yu, Y., Trouvé, a, Renaud, O., & Shorte, S. L. (2009). Isotropic high-resolution three-dimensional confocal micro-rotation imaging for non-adherent living cells. *Journal of microscopy*, *233*(3), 404-16. doi:10.1111/j.1365-2818.2009.03128.x

Lee, J.-H., Choi, W.-S., Lee, K.-H., & Yoon, J.-B. (2008). A simple and effective fabrication method for various 3D microstructures: backside 3D diffuser lithography. *Journal of Micromechanics and Microengineering*, *18*(12), 125015. doi:10.1088/0960-1317/18/12/125015

Lee, M. J., Lee, N. Y., Lim, J. R., Kim, J. B., Kim, M., Baik, H. K., & Kim, Y. S. (2006). Antiadhesion Surface Treatments of Molds for High-Resolution Unconventional Lithography. *Advanced Materials*, *18*(23), 3115-3119. doi:10.1002/adma.200601268

Lieu, V. H., House, T. a, & Schwartz, D. T. (2012). Hydrodynamic tweezers: impact of design geometry on flow and microparticle trapping. *Analytical chemistry*, *84*(4), 1963-8. doi:10.1021/ac203002z

Lim, D. S. W., Shelby, J. P., Kuo, J. S., & Chiu, D. T. (2003). Dynamic formation of ring-shaped patterns of colloidal particles in microfluidic systems. *Applied Physics Letters*, *83*(6), 1145. doi:10.1063/1.1600532

Losick, R., & Desplan, C. (2008). Stochasticity and cell fate. *Science (New York, N.Y.)*, *320*(5872), 65-8. doi:10.1126/science.1147888

Luo, L. W., Teo, C. Y., Ong, W. L., Tang, K. C., Cheow, L. F., & Yobas, L. (2007). Rapid prototyping of microfluidic systems using a laser-patterned tape. *Journal of Micromechanics and Microengineering*, *17*(12), N107-N111. doi:10.1088/0960-1317/17/12/N02

Mao, H., Arias-Gonzalez, J. R., Smith, S. B., Tinoco, I., & Bustamante, C. (2005). Temperature control methods in a laser tweezers system. *Biophysical journal*, *89*(2), 1308-16. Elsevier. doi:10.1529/biophysj.104.054536

Meador, M. A. B., Fabrizio, E. F., Ilhan, F., Dass, A., Zhang, G., Vassilaras, P., Johnston, J. C., et al. (2005). Cross-linking Amine-Modified Silica Aerogels with Epoxies : Mechanically Strong Lightweight Porous Materials, (2), 1085-1098.

Meyer, M. G., Fauver, M., Rahn, J. R., Neumann, T., Patten, F. W., Seibel, E. J., & Nelson, A. C. (2009). Automated cell analysis in 2D and 3D: A comparative study. *Pattern Recognition*, *42*(1), 141-146. doi:10.1016/j.patcog.2008.06.018

Miao, Q., Reeves, A. P., Patten, F. W., & Seibel, E. J. (2012). Multimodal 3D imaging of cells and tissue, bridging the gap between clinical and research microscopy. *Annals of biomedical engineering*, *40*(2), 263-76. doi:10.1007/s10439-011-0411-5

Miwa, M., Juodkazis, S., Kawakami, T., Matsuo, S., & Misawa, H. (2001). Femtosecond two-photon stereo-lithography. *Applied Physics A: Materials Science & Processing*, *73*(5), 561-566. doi:10.1007/s003390100934

Molloy, J. E., & Padgett, M. J. (2002). Lights, action: Optical tweezers. *Contemporary Physics*, *43*(4), 241-258. doi:10.1080/00107510110116051

Munson, B. R. (1971). Viscous incompressible flow between concentric rotating spheres. Part 1. Basic flow. *Journal of Fluid Mechanics*, *49*(2), 289-303. Retrieved from http://journals.cambridge.org/abstract_S0022112071002064

Nandakumar, V., Kelbauskas, L., Hernandez, K. F., Lintecum, K. M., Senechal, P., Bussey, K. J., Davies, P. C. W., et al. (2012). Isotropic 3D nuclear morphometry of normal, fibrocystic and malignant breast epithelial cells reveals new structural alterations. *PloS one*, *7*(1), e29230. doi:10.1371/journal.pone.0029230

Nandakumar, V., Kelbauskas, L., Johnson, R., & Meldrum, D. (2011). Quantitative characterization of preneoplastic progression using single-cell computed tomography and three-dimensional karyometry. *Cytometry. Part A : the journal of the International Society for Analytical Cytology*, *79*(1), 25-34. doi:10.1002/cyto.a.20997

Nieminen, T. a., Heckenberg, N. R., & Rubinsztein-dunlop, H. (2001). Optical measurement of microscopic torques. *Journal of Modern Optics*, *48*(3), 405-413. doi:10.1080/09500340108230922

Nilsson, J., Evander, M., Hammarström, B., & Laurell, T. (2009). Review of cell and particle trapping in microfluidic systems. *Analytica chimica acta*, *649*(2), 141-57. doi:10.1016/j.aca.2009.07.017

Omori, R., Kobayashi, T., & Suzuki, a. (1997). Observation of a single-beam gradient-force optical trap for dielectric particles in air. *Optics letters*, *22*(11), 816-8. Retrieved from http://www.ncbi.nlm.nih.gov/pubmed/18185672

O'Neil, A. T., & Padgett, M. J. (2002). Rotational control within optical tweezers by use of a rotating aperture. *Optics letters*, *27*(9), 743-5. Retrieved from http://www.ncbi.nlm.nih.gov/pubmed/18007918

Palik, E. D., Glembocki, O. J., Heard, I., Burno, P. S., & Tenerz, L. (1991). Etching roughness for (100) silicon surfaces in aqueous KOH. *Journal of Applied Physics*, *70*(6), 3291. doi:10.1063/1.349263

Park, T. G., Kim, J. J., Jung, S. H., Song, H. J., Chang, J. K., Han, D. C., & Yang, S. S. (2008). Fabrication of Megasonic-Agitated Module for Improving the Characteristics of Wet Etching. *Japanese Journal of Applied Physics*, *47*(6), 5262-5269. doi:10.1143/JJAP.47.5262

Paterson, L., MacDonald, M. P., Arlt, J., Sibbett, W., Bryant, P. E., & Dholakia, K. (2001). Controlled rotation of optically trapped microscopic particles. *Science (New York, N.Y.)*, *292*(5518), 912-4. doi:10.1126/science.1058591

Peterman, E. J. G., Gittes, F., & Schmidt, C. F. (2003). Laser-induced heating in optical traps. *Biophysical journal*, *84*(2 Pt 1), 1308-16. doi:10.1016/S0006-3495(03)74946-7

Pethig, R. (2010). Review Article-Dielectrophoresis: Status of the theory, technology, and applications. *Biomicrofluidics*, *4*(2). doi:10.1063/1.3456626

Pienta, K. J., & Coffey, D. S. (1991). Correlation of Nuclear Morphometry With Progression of Breast Cancer. *Cancer*, *68*, 2012-2016.

Ray, T., Zhu, H., & Meldrum, D. R. (2010). Deep reactive ion etching of fused silica using a single-coated soft mask layer for bio-analytical applications. *Journal of Micromechanics and Microengineering*, *20*(9), 097002. doi:10.1088/0960-1317/20/9/097002

Reyzer, M. L., Caldwell, R. L., Dugger, T. C., Forbes, J. T., Ritter, C. a, Guix, M., Arteaga, C. L., et al. (2004). Early changes in protein expression detected by mass spectrometry predict tumor response to molecular therapeutics. *Cancer research*, *64*(24), 9093-100. doi:10.1158/0008-5472.CAN-04-2231

Ross, D., Gaitan, M., & Locascio, L. E. (2001). Temperature measurement in microfluidic systems using a temperature-dependent fluorescent dye. *Analytical chemistry*, *73*(17), 4117-23. Retrieved from http://www.ncbi.nlm.nih.gov/pubmed/11569800

Sat, K., Shikida, M., Matsushima, Y., Yamashiro, T., Asaumi, K., Iriye, Y., & Yamamoto, M. (1998). Characterization of orientation-dependent etching properties of single-crystal silicon : effects of KOH concentration, *61*, 87-93.

Scheme, A. P. F.-T. (1996). The World Health Organization Classification of Adenohypophysial Neoplasms, 502-510.

Schermelleh, L., Heintzmann, R., & Leonhardt, H. (2010). A guide to super-resolution fluorescence microscopy. *The Journal of cell biology*, *190*(2), 165-75. doi:10.1083/jcb.201002018

Shao, L., Kner, P., Rego, E. H., & Gustafsson, M. G. L. (2011). Super-resolution 3D microscopy of live whole cells using structured illumination. *Nature methods*, *8*(12), 1044-6. doi:10.1038/nmeth.1734

Shelby, J. P., & Chiu, D. T. (2004). Controlled rotation of biological micro- and nano-particles in microvortices. *Lab on a chip*, *4*(3), 168-70. doi:10.1039/b402479f

Shelby, J. P., Mutch, S. a, & Chiu, D. T. (2004). Direct manipulation and observation of the rotational motion of single optically trapped microparticles and biological cells in microvortices. *Analytical chemistry*, *76*(9), 2492-7. doi:10.1021/ac035531v

Shen, C., & Floryan, J. M. (1985). Low Reynolds number flow over cavities. *Physics of Fluids*, *28*(11), 3191. doi:10.1063/1.865366

Shikida, M., Sato, K., Tokoro, K., & Uchikawa, D. (2000). Differences in anisotropic etching properties of KOH and TMAH solutions. *Sensors and Actuators A: Physical*, *80*(2), 179-188. doi:10.1016/S0924-4247(99)00264-2

Souza, N. (2011). Single-cell methods. *Nature Methods*, *9*(1), 35-35. Nature Publishing Group. doi:10.1038/nmeth.1819

Uvdal, K., Erlandsson, R., & Elwing, H. (1991). Structure of 3-Aminopropyl Triethoxy Silane on Silicon Oxide Preparation of APTES Surfaces, *147*(1).

Vlachopoulou, M.-E., Tserepi, a, Pavli, P., Argitis, P., Sanopoulou, M., & Misiakos, K. (2009). A low temperature surface modification assisted method for bonding plastic substrates. *Journal of Micromechanics and Microengineering*, *19*(1), 015007. doi:10.1088/0960-1317/19/1/015007

Voldman, J. (2006). Electrical forces for microscale cell manipulation. *Annual review of biomedical engineering*, *8*, 425-54. doi:10.1146/annurev.bioeng.8.061505.095739

Waits, C.M., Morgan, B., Kastantin, M., & Ghodssi, R. (2005). Microfabrication of 3D silicon MEMS structures using gray-scale lithography and deep reactive ion etching. *Sensors and Actuators A: Physical*, *119*(1), 245-253. doi:10.1016/j.sna.2004.03.024

Waits, Christopher M, Modafe, A., & Ghodssi, R. (2003). Investigation of gray-scale technology for large area 3D silicon MEMS structures, *170*.

White, F. M. (2006). Fluid Mechanics. *McGraw-Hill Series in Mechanical Engineering, 4th Edition*.

Wright, W. H., Sonek, G. J., Tadir, Y., & Berns, M. W. (1990). Laser trapping in cell biology. *IEEE Journal of Quantum Electronics*, *26*(12), 2148-2157. doi:10.1109/3.64351

Wu, M. C. (1997). Micromachining for Optical and Optoelectronic Systems, *85*(11), 1833-1856.

Yang, C.-R., Chen, P.-Y., Chiou, Y.-C., & Lee, R.-T. (2005). Effects of mechanical agitation and surfactant additive on silicon anisotropic etching in alkaline KOH solution. *Sensors and Actuators A: Physical*, *119*(1), 263-270. doi:10.1016/j.sna.2004.07.015

Zeng, J., Wang, J., Gao, W., Mohammadreza, A., Kelbauskas, L., Zhang, W., Johnson, R. H., et al. (2011). Quantitative single-cell gene expression measurements of multiple genes in response to hypoxia treatment. *Analytical and bioanalytical chemistry*, *401*(1), 3-13. doi:10.1007/s00216-011-5084-2

Zhang, H., & Liu, K.-K. (2008). Optical tweezers for single cells. *Journal of the Royal Society, Interface / the Royal Society*, *5*(24), 671-90. doi:10.1098/rsif.2008.0052

Zhang, Z., Zhao, P., Xiao, G., Watts, B. R., & Xu, C. (2011). Sealing SU-8 microfluidic channels using PDMS. *Biomicrofluidics*, *5*(4), 046503. doi:10.1063/1.3659016